2006

The Viscous Catenary

John Koulakis
Pomona College

The Viscous Catenary

John Koulakis

Advisor: Catalin Mitescu

A thesis submitted in partial fulfillment of
the requirements for the degree of
Bachelor of Arts in Physics
Pomona College

April 2006

Table of Contents

1. Abstract:

Variational techniques are used to develop a theory for the time evolution of a thin strand of viscous fluid suspended from two points. The shape of the strand is approximated to be a parabola and energy conservation is used to derive a differential equation modeling the change in height over time. Data is collected with a high resolution camera and a strobe light to obtain the position and shape of the strand over multiple intervals of time. Three very different and unexpected types of behaviors are observed depending on the initial thickness and shape of the filament. The approximation fits well with one type of behavior but variations in the thickness of the strand, and consequently in the center of mass, need to be factored in to predict the others.

2. Introduction and Background:

2.1 A Catenary:

A flexible cable of uniform density suspended from two endpoints in a uniform gravitational field hangs in a shape knows mathematically as a catenary, after the Latin word for "chain." The problem of finding this shape was proposed by Jacob Bernoulli and was independently found to be a hyperbolic cosine (Figure 2.1) by Leibniz, Huygens, and Johann Bernoulli in 1691. But if the material is fluid, the problem gets much more complicated. Surface tension and viscous forces compete with gravity to change the catenary-like shape over time.

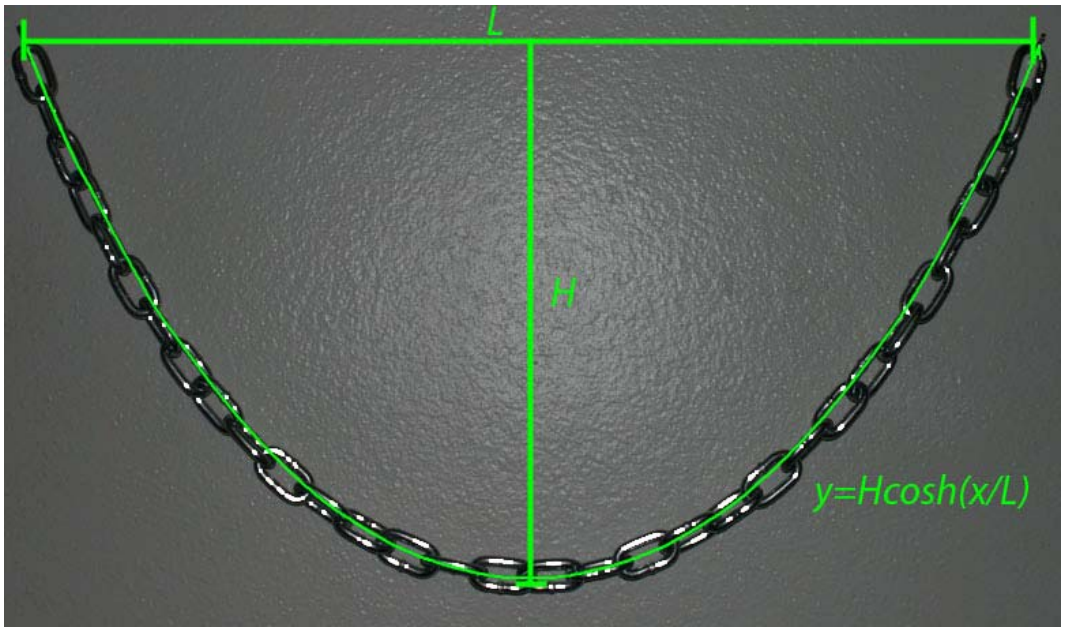

Figure 2.1: A chain hanging with a cosh function superimposed on it.

Recent studies in the area of fluid mechanics have focused on many different areas including the coiling of a falling viscous filament[5,7] and the folding of viscous sheets[4,8]. Y.M.Stokes *et al*[9] modeled the fall of a viscous drop. Brenner[1] and Chwalek[3] observed the deflection of viscous jets by asymmetric heating. In particular, L. Mahadevan and J. Teichman[6] at Harvard University investigated the dynamics of this "viscous catenary". More recently, F. Brochard-Wyart and P.-G. de Gennes[2] analyzed the problem from an energy perspective, which is intuitively easy to comprehend. We seek to continue and expand on Mahadevan, Teichman, Brochard-Wyart, and de Gennes' work by comparing the predictions of their theories to experimental data.

2.2 Teichman and Mahadevan's Analisys:

Mahadevan and Teichman assume that the filament is made of an incompressible Newtonian fluid, that gravity is the only body force acting on the filament, and that forces due to surface tension are small compared to viscous forces. They use a Lagrangian formulation where they define the coordinate s to be along the centerline of the unstretched filament and $\bar{s}(s,t)$ to be along the centerline of the stretched filament. The angle of the tangent to the centerline to the horizontal is $\theta(s,t)$, the vertical displacement of the centerline is $H(s,t)$, $h(s,t)$ is the diameter of the filament, $A(s,t) = \pi h^2/4$ is the cross-sectional area, $w = \rho g A$ is the weight per unit length of the undeformed filament where ρ is the density, and $\lambda(s,t) = \partial\bar{s}/\partial s$ is the local filament stretch. They also define $T(s,t)$ to be the tangential stress resultant (tension), $N(s,t)$ to be the normal stress resultant (shear), and $M(s,t)$ to be the torque resultant.

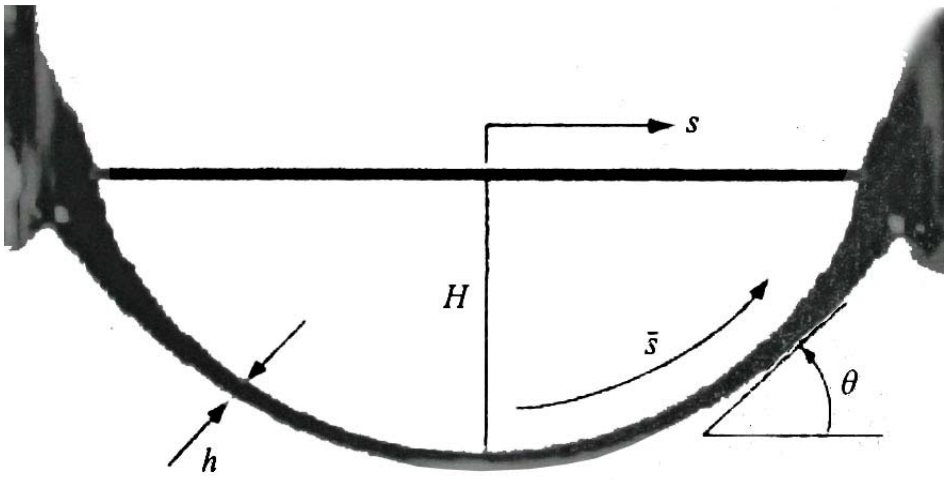

Figure 2.2: Mahadevan and Teichman's[5] definition of variables.

If the filament falls slowly and inertia can be neglected, the equations for the balance of forces and torques are

$$T_x - N\theta_x - w\sin\theta = 0, \qquad 2.1$$

$$N_x + T\theta_s - w\cos\theta = 0, \qquad 2.2$$

$$\text{and} \qquad M_s + N = 0. \qquad 2.3$$

For a Newtonian fluid, the continuity and closure relations are

$$(A\lambda)_t = 0\,, \tag{2.4}$$

$$T = 3\mu A(\ln\lambda)\ , \tag{2.5}$$

$$\text{and} \qquad M = D\theta_{st}\,, \tag{2.6}$$

where μ is the viscosity and $D = 3\mu A^2/4\pi$ is the bending stiffness of the filament. From these equations, Mahadevan and Teichman derive a nonlinear integro-differential equation for $\theta(x,t)$:

$$D\theta_{xxt} - \frac{3\mu A}{L}\theta\int_0^{L/2}(\theta^2)_t\,dx = -wx\,, \tag{2.7}$$

which can be written in the dimensionless form as,

$$\varepsilon^3\frac{\theta_{xxt}}{32} - \varepsilon\frac{\theta}{2}\int_0^{1/2}(\theta^2)_t\,dx = -x\,, \tag{2.8}$$

where $\varepsilon = h/L$, when all lengths are rescaled by the initial length L and by a characteristic time $3\pi\mu h/2w$, which they determined by balancing gravity and viscosity. The first term represents the filament's resistance to bending, and is dominant at small deformations. The second term is the filament's resistance to stretching, which becomes more dominant as time progresses, except for the region near the endpoints where the bending deformation is still large. For small deformations, we can ignore the second term and the solution becomes

$$\theta(x,t) = -\frac{wt}{24D}\left[\left(\frac{L}{2}\right)^2 - x^2\right]^2. \tag{2.9}$$

They calculate a $t_c \sim \mu h^5/wL^4$ beyond which the stretching deformation cannot be ignored. The value for t_c is on the order of microseconds for the filaments they observed, so this regime is very difficult to see. For $t > t_c$, the bending term becomes small except for a bending boundary layer near the endpoints of width $\delta \sim (\mu h^5/wL)^{1/3}\,t^{-1/3}$, which becomes smaller as time progresses. The exact solution to the stretching term is

$$\theta(x,t) = \left(\frac{12w}{\mu AL^2}\right)^{1/3}xt^{1/3}, \qquad x\in[0, L/2-\delta]\,. \tag{2.10}$$

As the filament stretches, it thins. These equations imply that the cross-sectional area is given by

$$A(s,t) = A_0(s) - \frac{\rho g t}{3\mu}\int_0^s A_0(s)ds\,. \qquad 2.11$$

The time when the filament breaks is determined by setting *A(s,t*)* equal to zero, which gives

$$t^*(s) = \frac{3\mu A_0(s)}{pg\int_0^s A_0(s)}\,. \qquad 2.12$$

The position of the break is in the region between the bending boundary layer and the stretching solution.

2.3 F. Brochard-Wyart and P.G. de Gennes' Analysis:

Brochard-Wyart and de Gennes[2] begin by pointing out that the filament is inherently unstable by a process similar to the Rayleigh-Plateau instability. If the diameter of the filament is not completely uniform, it will continue to thin in any region where its diameter is slightly smaller. If the diameter, d, is slightly perturbed to $d + u$, its Laplace pressure p becomes

$$p = \frac{2\gamma}{d} \to \frac{2\gamma}{d+u} \approx \frac{2\gamma}{d} - \frac{2\gamma u}{d^2} = p_0 + p_1\,, \qquad 2.13$$

where γ is the surface tension. The approximation here is valid only when u is small compared to d. This difference in pressure causes a flow along the thread axis. If there is no body force acting on the strand, the Navier-Stokes equation becomes

$$0 = \rho\frac{\partial U}{\partial t} = \eta\frac{\partial^2 U}{\partial x^2} - \frac{\partial p}{\partial x}\,, \qquad 2.14$$

where U is the velocity of the fluid and η is the viscosity. Integrating this yields

$$\frac{\partial U}{\partial x} = \frac{1}{\eta}p_1 = \frac{2\gamma}{\eta d^2}u\,. \qquad 2.15$$

For an incompressible fluid, we have

$$\frac{\partial U}{\partial x} = -\frac{2\dot{u}}{d}, \qquad 2.16$$

and setting this equal to equation 2.15 gives the relation

$$\dot{u} = \frac{\gamma}{\eta d}u\,, \qquad 2.17$$

indicating an exponential growth rate with characteristic time $\tau_R = \frac{\eta d}{\gamma}$, the Rayleigh growth time, the timescale over which the fluid spontaneously begins to break up. Any discussion of the evolution of the filament should cover times much less than τ_R.

Since we are concerned with finding a timescale over which the fluid breaks, we are ultimately interested in the behavior when *d* approaches zero. As this happens, the approximation made in equation 2.13 breaks down, and this may lead to a significantly different τ_R.

Whereas Teichman and Mahadevan predict the evolution of the filament from a force perspective, Brochard-Wyart and de Gennes focus on energy considerations. For a filament that falls slowly, the energy gained from the decrease in potential must be equal to the energy dissipated in the fluid by stretching. This dissipation is given by

$$T\dot{S} = \Omega \eta \dot{\varepsilon}^2, \tag{2.18}$$

where $T\dot{S}$ is the change in entropy per unit time, $\Omega = \frac{M}{\rho}$ is the volume of the filament, M is the mass of the filament, ρ is the density, η is the dynamic viscosity, and $\dot{\varepsilon}$ is the strain rate. We recognize that $\eta\dot{\varepsilon}$ is the viscous stress, which multiplied by the strain rate gives the dissipation per unit volume. Setting equation 2.18 equal to the change in potential gives,

$$\dot{V} = Mg\dot{\bar{y}}, \tag{2.19}$$

where g is the acceleration of gravity and $\dot{\bar{y}}$ is the time rate of change of the center of mass of the system. For small-curved deformations, the position center of mass is 2/3 of the maximum deflection. By a scaling argument Brochard-Wyart and de Gennes predict a growth law proportional to $t^{1/3}$ (we derive this more quantitatively by the analysis carried out in section 3.1). For deformations *L(t)* very large compared to the separation of the points of suspension, the center of mass is located at $L/4$ and Brochard-Wyart and de Gennes easily derive an asymptotic growth law of the form

$$\frac{1}{L(t_1)} - \frac{1}{L(t)} = \frac{g}{4\nu}(t - t_1), \tag{2.20}$$

where $\nu = \frac{\eta}{\rho}$ is the kinematic viscosity and L is the length of the filament at time t. Here, t_1 is an arbitrary transition time where the regimes of strong and small deformations meet. Equation 2.20 indicates that the filament length diverges at a finite time.

This gives a simple understanding of the system that is useful in developing an intuition of the mechanics involved. However, this does not take into account the effects of any variation in the diameter of the filament. Also, this assumes the filament falls slowly and that only a small fraction of the energy is kinetic, which is not the case for thick filaments or for filaments that are near the breaking point.

In chapter 3, we extend this analysis by assuming functional forms for the shape of the filament and working out the predictions. We work out in detail the implications of this for a filament that has the form of an arc of a large circle and for a parabolic filament.

3. Theory:

3.1 Small Deformations:

Following F. Brochard-Wyart and P.-G de Gennes'[2] qualitative analysis, we make more quantitative predictions of how the filament should evolve. We approximate the filament as being an arc of a large circle. Let R be the radius of the circle, L be the length of the filament (initially L_0), θ_m be the angle spanned by the filament, and y_m be distance the middle of the filament has fallen.

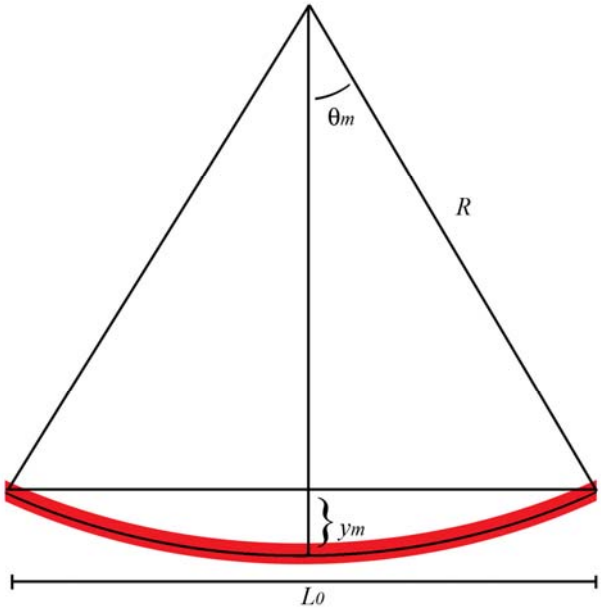

Figure 3.1: Diagram of Filament

Then

$$\frac{L_0}{2R} = \sin(\theta_m), \tag{3.1a}$$

$$L = 2R\theta_m, \tag{3.1b}$$

and Euclidean geometry tells us that

$$\frac{L_0^2}{4} = (2R - y_m)y_m \approx 2Ry_m. \tag{3.1c}$$

For small deformations, the strain is

$$\varepsilon = \frac{L - L_0}{L_0} = \frac{2R\theta_m - 2R\sin(\theta_m)}{L_0} \approx \frac{R\theta_m{}^3}{3L_0} = \frac{\theta_m{}^2}{6}, \qquad 3.2$$

and the strain rate is

$$\dot{\varepsilon} = \frac{\theta_m \dot{\theta}_m}{3}. \qquad 3.3$$

The heat dissipation in the fluid, as in equation 2.18, is given by

$$T\dot{S} = \frac{M}{\rho}\eta\dot{\varepsilon}^2, \qquad 3.4$$

where M is the mass of the fluid, ρ is the density, and η is the dynamic viscosity. Since we are assuming the deformation is small and the filament is falling slowly, the heat dissipated must be equal to the change in potential.

Assuming a uniform cross section, the position of the center of mass of the filament relative to the initial position of the midpoint is given by

$$\bar{y} = \frac{2R^2\rho\int_0^{\theta m}(\cos(\theta_m) - \cos(\theta))d\theta}{R\rho\int_{-\theta m}^{\theta m} d\theta} = R(\cos(\theta_m) - \frac{\sin(\theta_m)}{\theta_m}) = \frac{L_0}{2}(\cot(\theta_m) - \frac{1}{\theta_m}). \qquad 3.5a$$

Approximating $\sin(\theta) \approx \theta - \frac{\theta^3}{6}$ and $\cos(\theta) \approx 1 - \frac{\theta^2}{2}$, and using equations 3.1a, 3.1b, and 3.1c, this becomes

$$\bar{y} \approx \frac{R\theta_m^2}{3} = \frac{2}{3}y_m, \qquad 3.5b$$

from which we also see that

$$y_m = \frac{L_0}{4}\theta_m. \qquad 3.5c$$

Therefore, the potential energy is

$$V = -\frac{2}{3}y_m Mg \approx -\frac{L_0\theta_m}{6}Mg, \qquad 3.6$$

when written in terms of θ_m.

Setting the heat dissipation equal to the change in potential, we get

$$\frac{M}{9\rho}\eta\theta_m^2\dot{\theta}^2 = \frac{L_0\dot{\theta}_m}{6}Mg \qquad \rightarrow \qquad \theta_m^2 d\theta_m = \frac{3L\rho g}{2\eta}dt. \qquad 3.7$$

Integrating yields

$$\theta_m^3 = \frac{9}{2\nu} L_0 g t \,. \qquad 3.8$$

So for small deformations, y_m grows as $t^{1/3}$. To arrive at equation 3.8, we used the small angle approximation and assumed that the filament was an arc of a circle and that it did not stretch much compared to its initial length, which are valid assumptions for small deformations. This is in agreement with the results predicted by Brochard-Wyart and de Gennes.

3.2 Intermediate Deformations:

To try and predict the behavior over a longer period of time, we cannot work within the small angle approximation or assume that the filament does not stretch much compared to its initial length. Again we have $L = R\theta$ and $\frac{L_0}{2} = R\sin(\theta)$. The strain rate becomes

$$\dot{\varepsilon} = \frac{\dot{L}}{L} = \frac{\dot{R}}{R} + \frac{\dot{\theta}}{\theta} = (-\cot(\theta) + \frac{1}{\theta})\dot{\theta}\,, \qquad 3.9$$

when we use equation 3.1a to replace R with θ. Notice that this is the negative of the function of theta that appears in the exact equation for the center of mass in 3.5a. Let

$$J(\theta) = (\cot(\theta) - \frac{1}{\theta})\,. \qquad 3.10$$

Equating the change in potential with the change in entropy yields the equation

$$\frac{M}{\rho}\eta J^2(\theta)\dot{\theta} = \frac{MgL_0}{2}J'(\theta) \quad \rightarrow \quad \int \frac{J^2(\theta)}{J'(\theta)}d\theta = \frac{L_0 g}{2\nu}dt\,, \qquad 3.11$$

which is integrable numerically. This approximation appears good while the filament is approximately an arc of a circle and seems to hold until θ is about 60 degrees. In this regime we note that the maximum deflection is comparable to but less than L_0. To describe the motion further into the region where y_m exceeds L_0, we need a better approximation.

3.3 Parabolic Approximation:

Now we assume that the function is in the shape of a parabola of the form

$$y = -y_m(1-\frac{4x^2}{{L_0}^2}) = -L_0 h(1-\frac{4x^2}{{L_0}^2}), \tag{3.12}$$

where $h = \frac{y_m}{L_0}$ is a unitless measure of the height. This function always equals zero at $x = \pm\frac{L_0}{2}$ and has height y_m. Then the distance along the filament is given by

$$L = \int_{-L_0/2}^{L_0/2} \sqrt{1+\frac{64h^2x^2}{{L_0}^2}}dx = L_0\int_0^1 \sqrt{1+16h^2u^2}\,du = L_0F(h), \tag{3.13}$$

where we define $u = \frac{2x}{L_0}$ and $F(h) = \int_0^1 \sqrt{1+16h^2u^2}\,du$. Taking the derivative of this with respect to time, we get

$$\dot{L} = L_o\dot{h}\int_0^1 \frac{16hu^2}{\sqrt{1+16h^2u^2}}du = L_0\dot{h}W(h), \tag{3.14}$$

where $W(h) = \int_0^1 \frac{16hu^2}{\sqrt{1+16h^2u^2}}du$. This implies a strain rate of

$$\dot{\varepsilon} = \frac{\dot{L}}{L} = \frac{W(h)}{F(h)}\dot{h}. \tag{3.15}$$

The center of mass of this parabola is given by

$$\bar{y} = \frac{{L_0}^2 h\int_0^1 (1-u^2)\sqrt{1+16h^2u^2}\,du}{L_0\int_0^1 \sqrt{1+16h^2u^2}\,du} = \frac{L_0hP(h)}{F(h)}. \tag{3.16}$$

where $P(h) = \int_0^1 (1-u^2)\sqrt{1+16h^2u^2}\,du$. Graphing $\bar{y}$ as a function of *h* (Graph 3.1), we see that the center of mass starts off at 2/3 of the height and approaches 1/2 of the height in the limit that *L* is long, as expected. We also see that it is changing rapidly initially, which implies that the small angle and circular approximations quickly become bad. When *h* is 0.5, $\bar{y}$ has already changed by about 10%.

Taking the time derivative of the center of mass, we get

$$\dot{\bar{y}} = L_0 \frac{F(P+hQ) - hPW}{F^2}\dot{h}, \tag{3.17}$$

$$\text{where} \quad Q(h) = \frac{\partial P}{\partial h} = \int_0^1 \frac{16h(1-u^2)u^2}{\sqrt{1+16h^2u^2}}du\,. \tag{3.18}$$

Solving analytically for F, W, P, and Q in Mathematica,

$$F(h) = \int_0^1 \sqrt{1+16h^2u^2}\,du = \frac{1}{2}\sqrt{1+16h^2} + \frac{1}{8h}\sinh^{-1}(4h), \tag{3.19}$$

$$W(h) = \int_0^1 \frac{16hu^2}{\sqrt{1+16h^2u^2}}du = \frac{1}{2h}\sqrt{1+16h^2} - \frac{1}{8h^2}\sinh^{-1}(4h), \tag{3.20}$$

$$P(h) = \int_0^1 (1-u^2)\sqrt{1+16h^2u^2}\,du$$

$$= -\frac{1}{512h^3}[4h\sqrt{1+16h^2}(1-32h^2) - (64h^2+1)\sinh^{-1}(4h)], \tag{3.21}$$

and $$Q(h) = \int_0^1 \frac{16h(1-u^2)u^2}{\sqrt{1+16h^2u^2}}du$$

$$= \frac{1}{512h^4}[4h\sqrt{1+16h^2}(32h^2+3) - (64h^2+3)\sinh^{-1}(4h)]\,. \tag{3.22}$$

Equating the heat dissipation with the change in potential yields,

$$\frac{M}{\rho}\eta\dot{\varepsilon}^2 = Mg\dot{\bar{y}}, \tag{3.23}$$

and substituting in equations 3.15 and 3.17 we get the differential equation

$$\frac{W^2}{F(P+hQ) - hPW}dh = \frac{gL_0}{\nu}dt\,. \tag{3.24}$$

Since we know every function here, we can use Simpson's rule to numerically solve this equation and make predictions for the evolution of the filament as shown in Graphs 3.2 and 3.3.

When integrated, we can write the left side of this equation as being a constant, α, multiplied by a function of h, which we know from our other approximations is h^3 for small h, yielding

$$\alpha h^3 = \frac{gL_0}{\nu} t \,. \qquad 3.25$$

Defining $t_g = \frac{\alpha \nu}{gL_0}$, we can define a dimensionless time $\tau = \frac{t}{t_g}$ so that equation 3.25 becomes

$$h^3 = \tau \,, \qquad 3.26$$

and we can rewrite equation 3.24 as

$$\frac{1}{\alpha} \frac{W^2}{F(P + hQ) - hPW} dh = d\tau \,. \qquad 3.27$$

To find α, we can look at equation 3.27 in the limit that *h* is small and find the constant that emerges. In this limit, equation 3.13 becomes

$$L = L_0 \int_0^1 \sqrt{1 + 16h^2u^2}\, du \approx L_0 \int_0^1 (1 + \frac{8}{3}u^2h^2) du = L_0 (1 + \frac{8}{3}h^2) \qquad 3.28$$

and therefore,

$$\dot{L} = L_0 \frac{16}{3} h\dot{h} \quad \text{and} \quad \dot{\varepsilon} = \frac{L}{L_0} = \frac{16}{3} h\dot{h} \,. \qquad 3.29$$

We have already seen that $\dot{\bar{y}}$ reduces to $\frac{2}{3} L_0 \dot{h}$, which implies that

$$\frac{256}{9} \frac{M}{\nu} \eta h^2 \dot{h}^2 = MgL_0 \frac{2}{3} h\dot{h} \,, \qquad 3.30$$

$$\text{and} \qquad \frac{128}{9} h^3 = \frac{gL_0}{\nu} t \,. \qquad 3.31$$

Therefore, $\alpha = \frac{128}{9} \approx 14.22$ and $\tau = \frac{9gL_0}{128\nu} t$.

Graphing ln *h* against ln *τ* (Graph 3.4), we see a slope of 1/3 early on in agreement with the results predicted by Teichman, Mahadevan, Brochard-Wyart and de Gennes. According to the long term predictions of Brochard-Wyart and de Gennes, a graph of 1/*L* against *τ* (Graph 3.5) should be linear for long *L*, with a slope of $-\frac{\alpha}{4} \approx 3.555$ and an intercept of $(\frac{\alpha}{4}\tau_1 + \frac{1}{L(\tau_1)})$. This is exactly the slope we see. Graphing the value of the intercept for different values of *τ* (Graph 3.6), we see that it converges to a value of

around .7831, the intercept we are seeing. As expected, there is no clear cut time where the regimes of small and strong deformation meet, but rather as τ increases, the more dominant the regime of strong deformation becomes.

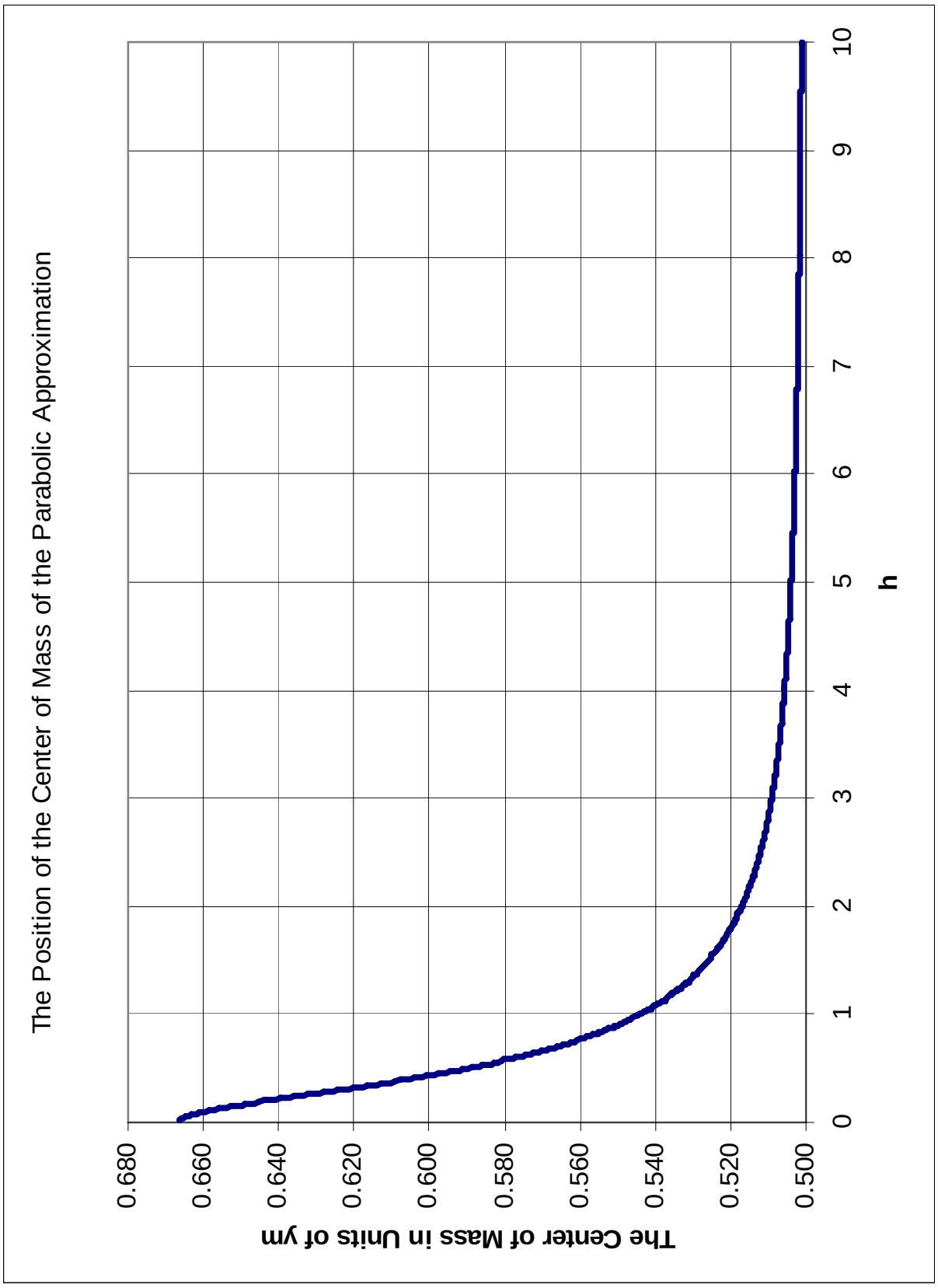

Graph 3.1: The position of the center of mass as a function of *h*.

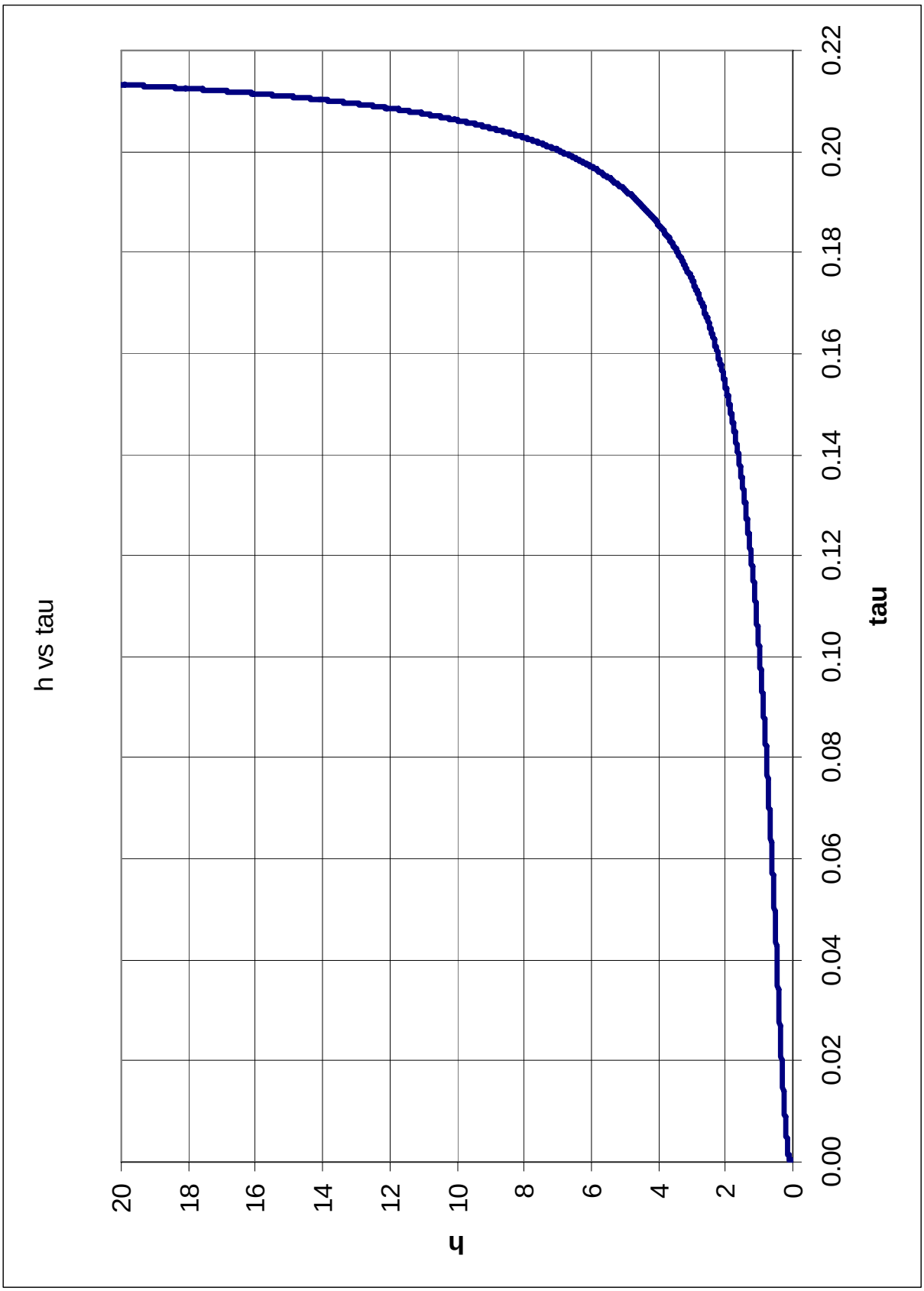

Graph 3.2: h as predicted by the parabolic approximation.

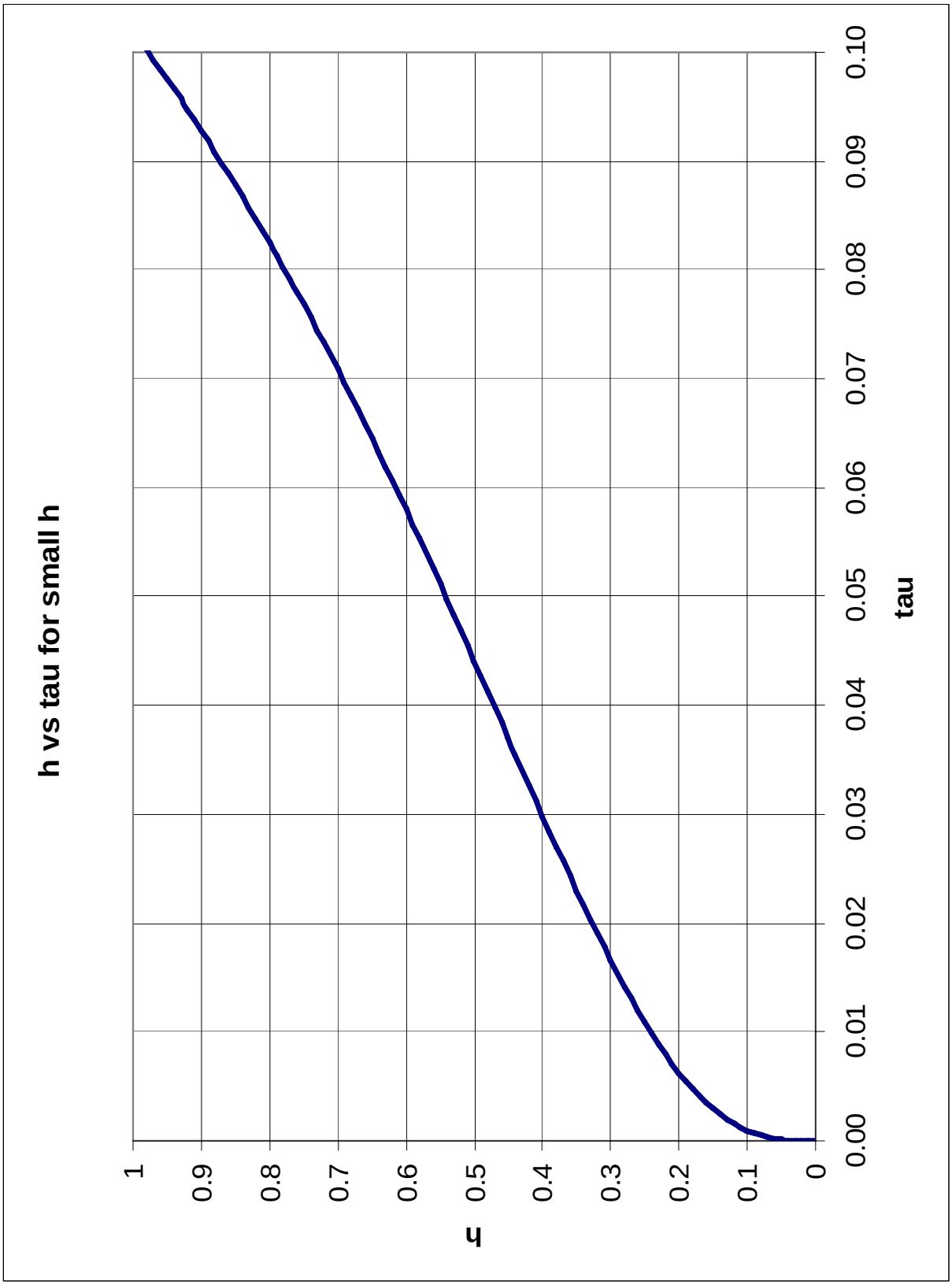

Graph 3.3: h as predicted by the parabolic approximation early on.

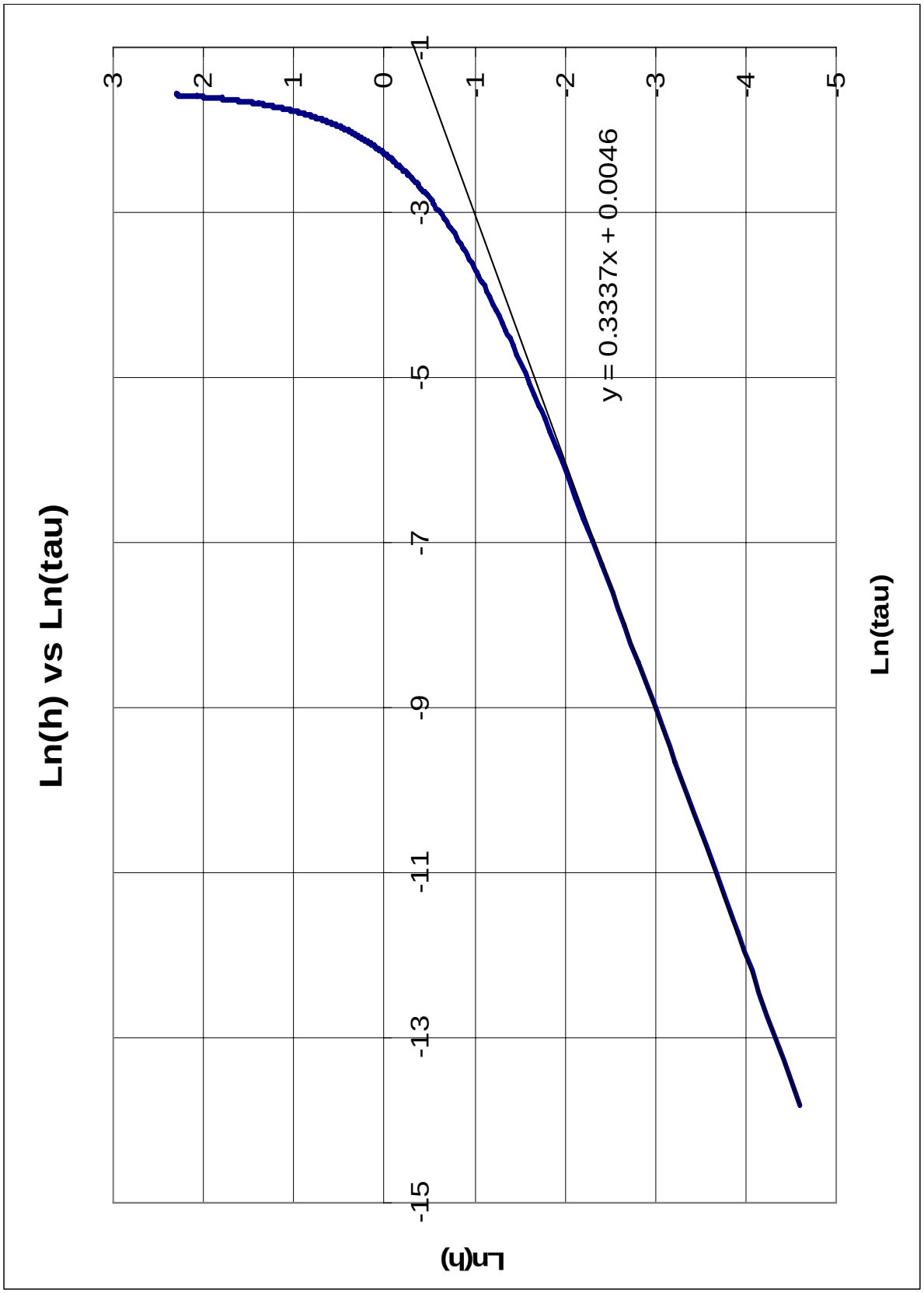

Graph 3.4: Comparison with Brochard-Wyart and de Gennes' short-term predictions.

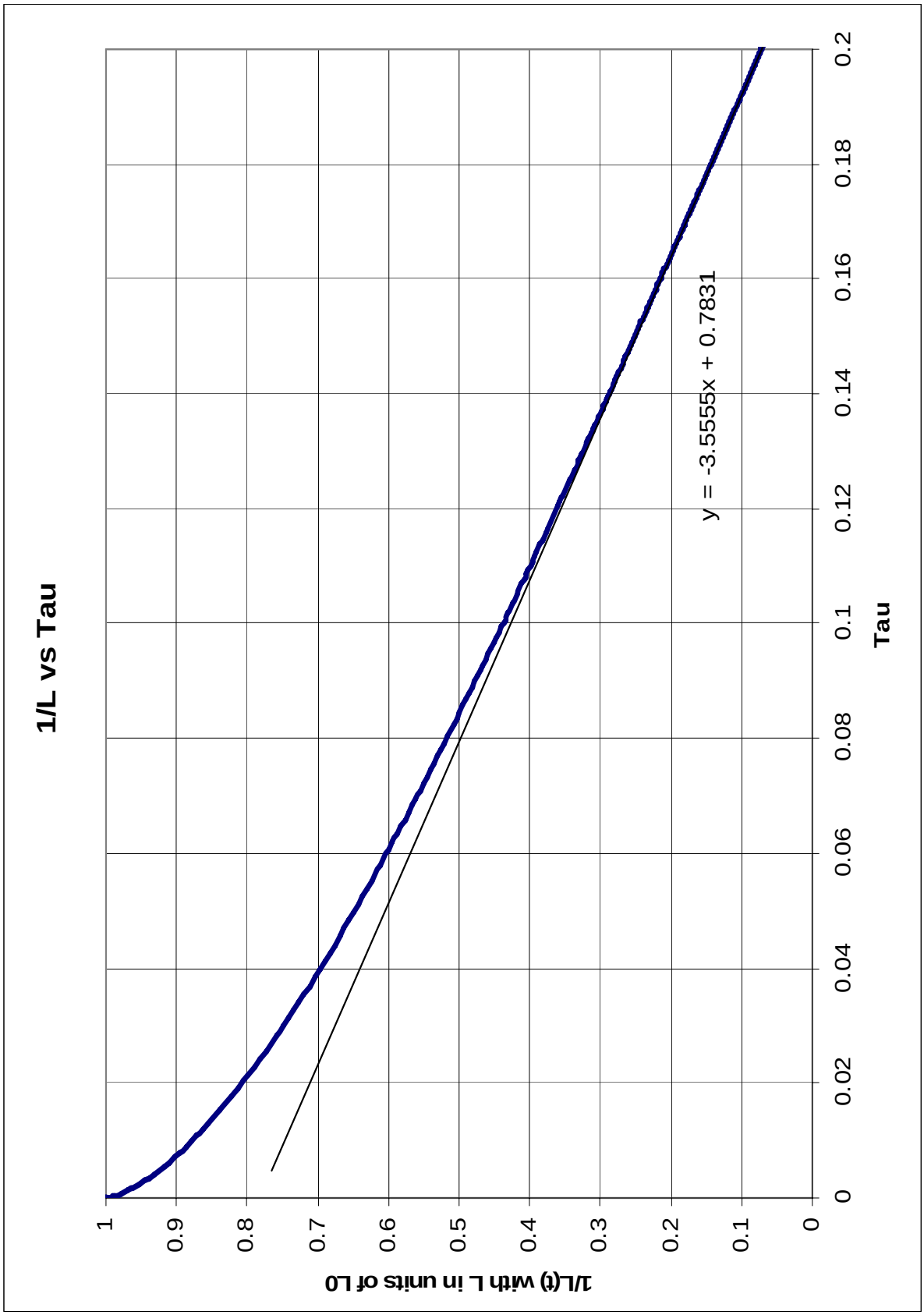

Graph 3.5: Comparison with Brochard-Wyart and de Gennes' long-term predictions.

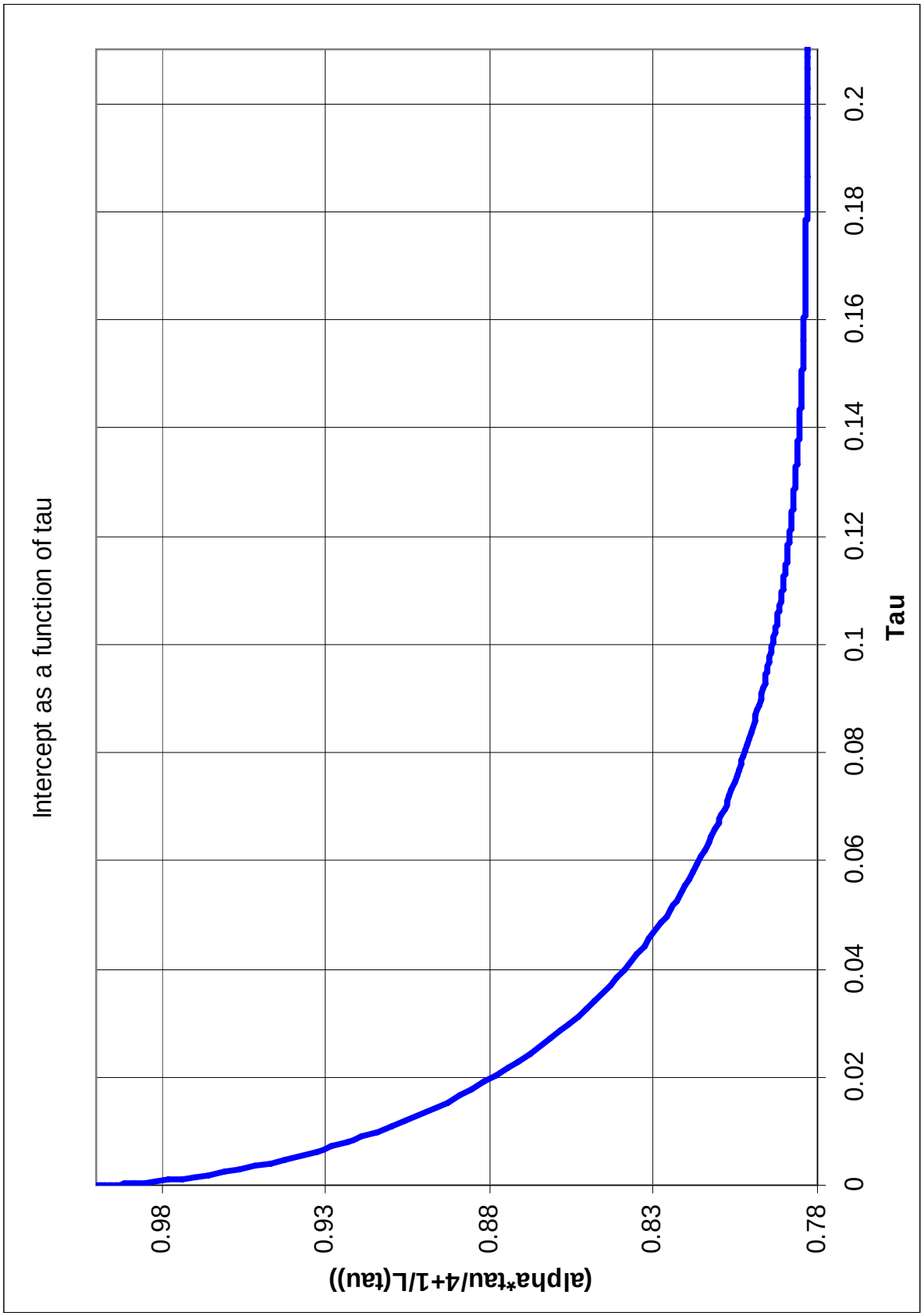

Graph 3.6: As tau increases, the value of the intercept converges to what we are seeing.

4. The Development of our Procedure:

4.1 Apparatus:

When I began working on this in June 2005, my goal was to find a function that accurately describes the shape of the falling filament over time. I needed a repeatable technique of creating a filament that would allow me to change parameters such as the filament's radius and the separation between its endpoints. Fortunately this was provided for me by the hard work of Chris Billingham and Glenn Flohr, who during the previous summer conceived and built the apparatus shown in Figs 4.1 and 4.2.

Figure 4.1: Apparatus in the open position (high resolution on CD).

Figure 4.2: Assorted tubes (high resolution on CD).

The apparatus consists of two plastic tubes that slide over a stationary stainless steel rod. The tubes are filled with silicone oil (Clearco 100M Silicone "O" Ring Lubricant which has a kinematic viscosity of ν = 100,000 centistokes = 0.1 m^2/s) and joined at the middle, forming a continuum of fluid. When they are released, rubber bands pull the tubes apart, sliding them over the steel rods which push the oil out. A filament of oil is formed between the tubes. By using tubes of different diameter, we can adjust the thickness of the filament. We have tubes at 1/8 in, 3/16 in, 1/4 in, and 5/16 in diameters. Also, changing the tension of the rubber bands causes the tubes to pull apart at a different speed, changing the thickness of the filament. The apparatus allows for 5 different tension settings, which can significantly change how the filament is formed. Placing a clip on the steel rods allows for adjusting how far apart the tubes are pulled, which also greatly changes the shape of the filament.

4.2 Different Behaviors:

Over the summer of 2005, I experimented with the various parameters and got a good feel for how the filament evolves under various circumstances. It became clear that there were two very distinct phases or regimes in the evolution of the filament. All would start essentially straight and would begin to droop or fall from the middle, forming a "u" shape that would become deeper and longer as it fell. I call this the "falling" phase (see video "Falling"). As expected, some filaments would continue falling in this manner until they hit the tray below. Interestingly however, for thinner filaments, a point was reached where they would stop falling all together and they seemed to hang in a stationary "u" shape, evolving very slowly. After a few moments they began to pull apart in the middle and square off at the edges. Eventually the sides became very close to vertical, connected by an increasingly thin and straight horizontal filament by "corners" with a very small radius of curvature. The thin filament would continue pulling apart, eventually breaking in the middle. I call this the "breaking" phase (see video "Breaking"). Sometimes, while in the breaking phase, the middle of the filament would move up higher than the sides supporting it, forming a "w" shape just before rupturing (see video "w"). Figures 4.3 – 4.5 show examples of the falling and breaking phases and the "w" shape. Figures 4.3 and 4.5 are a series of frames taken from a video. Figure 4.4

is a picture taken with a strobe light (the technique is fully described later in section 4.4). Notice in Figure 4.4 that the middle of the filament actually moved upwards in the breaking phase while it was pulling apart until it flattened out. The flattening is not a result of the sides falling faster than the middle.

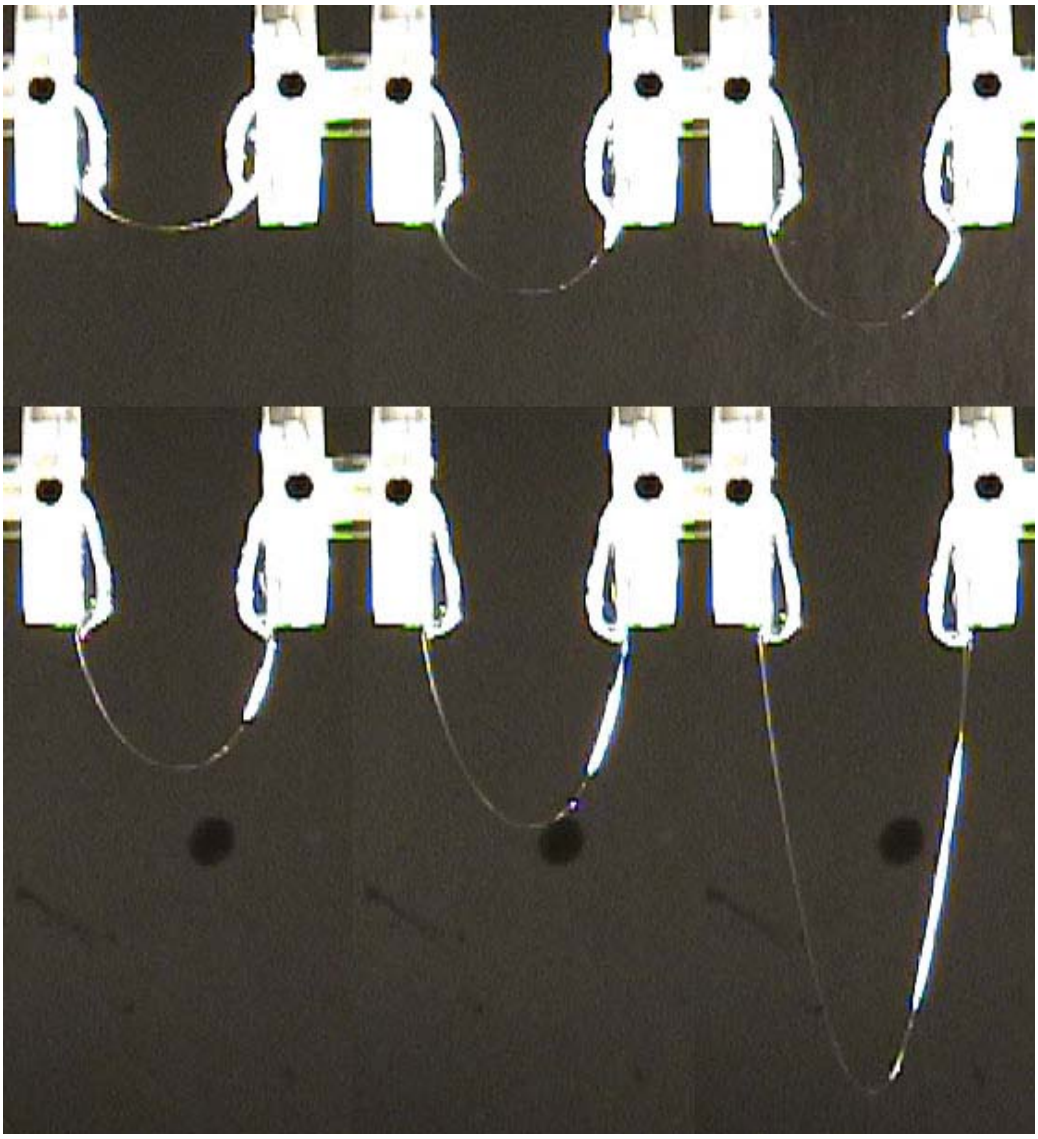

Figure 4.3: Example of "Falling."

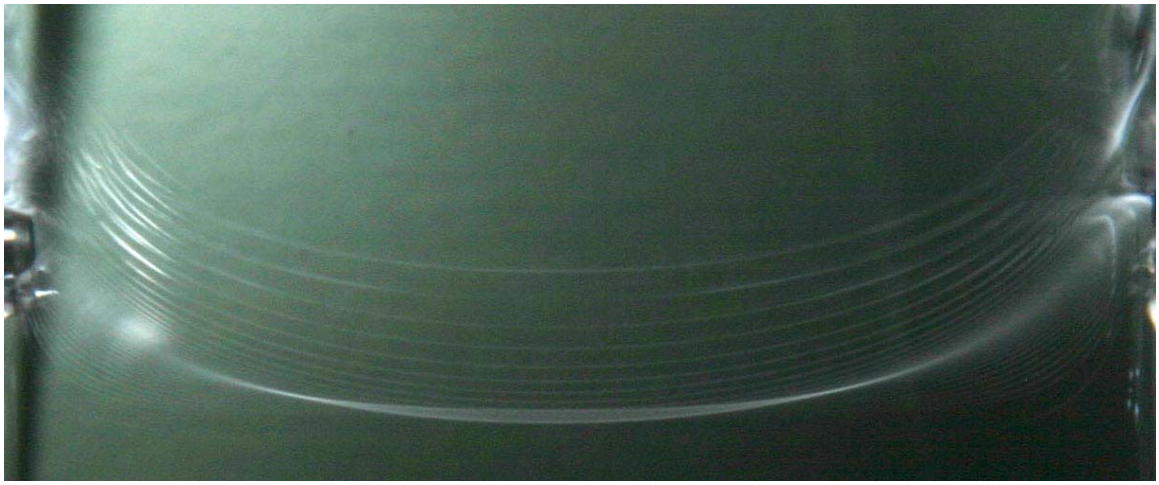

Figure 4.4: Example of "Breaking"

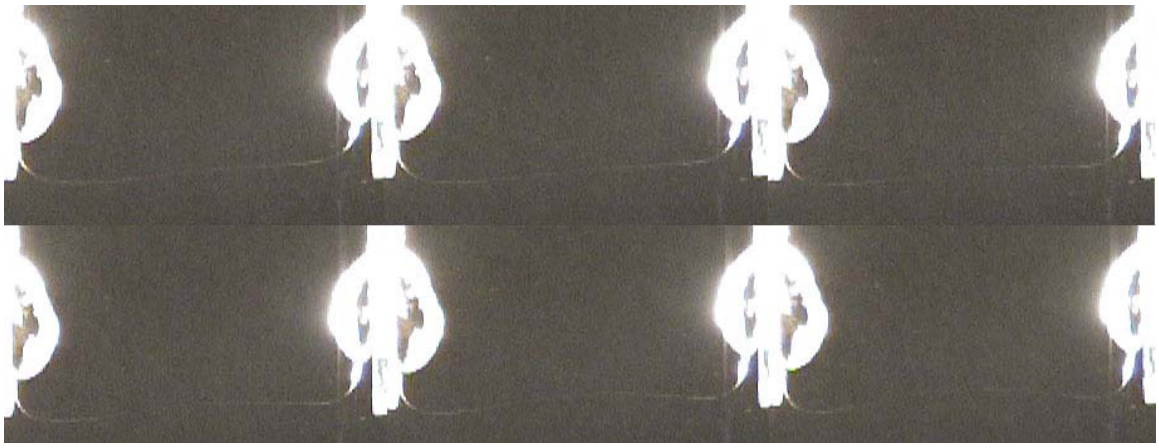

Figure 4.5: Example of a "w."

4.3 Data Capture - Problems and Solutions:

The runs were videotaped with a *Sony DCR-TRV18 Digital Handycam* which is capable of recording at 30 frames per second at a resolution of 640 x 480. Since the viscosity of the oil is so high, it takes several seconds for it to completely evolve, yielding a lot of frames to analyze. A piece of black construction paper was used for the background and a suitable arrangement for the position of the light was found by trial and error. A good arrangement for the light was placing it on the countertop below the level of the oil, between the oil and the construction paper, pointing upwards and a little back towards the camera. This gave a good contrast between the background and the oil in the video. Using firewire, the video was captured directly into *iMovie 3.03* running on a G4

laptop with *Mac OS X 10.3.6*. *iMovi*e allows for the extraction of individual frames from the video, which were imported to *ImageJ 1.33u*. Clicking along the filament in *ImageJ* would give a set of (x,y) coordinates along the curve, which were then analyzed in *Microsoft Excel*.

Two problems quickly became apparent with this process of digitizing the filament. The video resolution of 640x480 is not fine enough to yield precise data points along the filament. At this resolution, the thickness of the vein cannot be measured with sufficient precision, as the whole width of the vein is spanned by only three to four pixels, which leads to high uncertainties. In addition, it is difficult to ascertain the shape of the filament early on in the evolution process because the trough of the vein is only a couple pixels lower than the sides of the vein. Also, manually clicking all along the filament to get data points, especially when it is not clear where the boundaries are because of the poor resolution, is very time consuming, imprecise, and inefficient. It was clear that a method of capturing data at a higher resolution, while maintaining a reasonable frame rate, was necessary.

Purchasing a high resolution video camera, the obvious solution at the time, was significantly outside of our budget. Fortunately, we have a still, digital SLR camera available, a *Canon EOS 10D*, that is capable of taking pictures at a resolution of 3072x2048. However, the still camera is not capable of taking pictures in rapid succession at a suitable rate for our purposes. Dr. Mitescu suggested a very clever solution to this problem – use a strobe light. A strobe light flashing at a sufficient speed in a dark room with the still camera set to a time exposure allows for capturing an image of the filament at multiple instances in time on a single picture.

After overcoming some significant initial obstacles, this technique now works well for capturing the motion of the oil. Depending on where the strobe is positioned, different parts of the vein reflect the light into the camera. Also, as the vein falls, the parts that reflect light change. If the strobe is to the side of the oil, the vertical pieces reflect back (Fig 4.6). If the strobe is centered in front of the oil but above or below the camera, only the horizontal sections reflect light towards the camera. The arrangement that works the best is to position the strobe as close to the filament as possible, just out of the field of view of the camera. It is placed slightly to the side and above the initial level

of the filament. This works very well for illuminating the oil early, while it is still close to the strobe. As it falls, however, it looses brightness. I have not been able to illuminate the oil sufficiently so that it is visible during the full fall to the tray below using only the strobe we have, so we decided to focus on the region best visible. Using sufficiently small separations and thin filaments, we can produce any behavior we are interested in, in the small, well illuminated region.

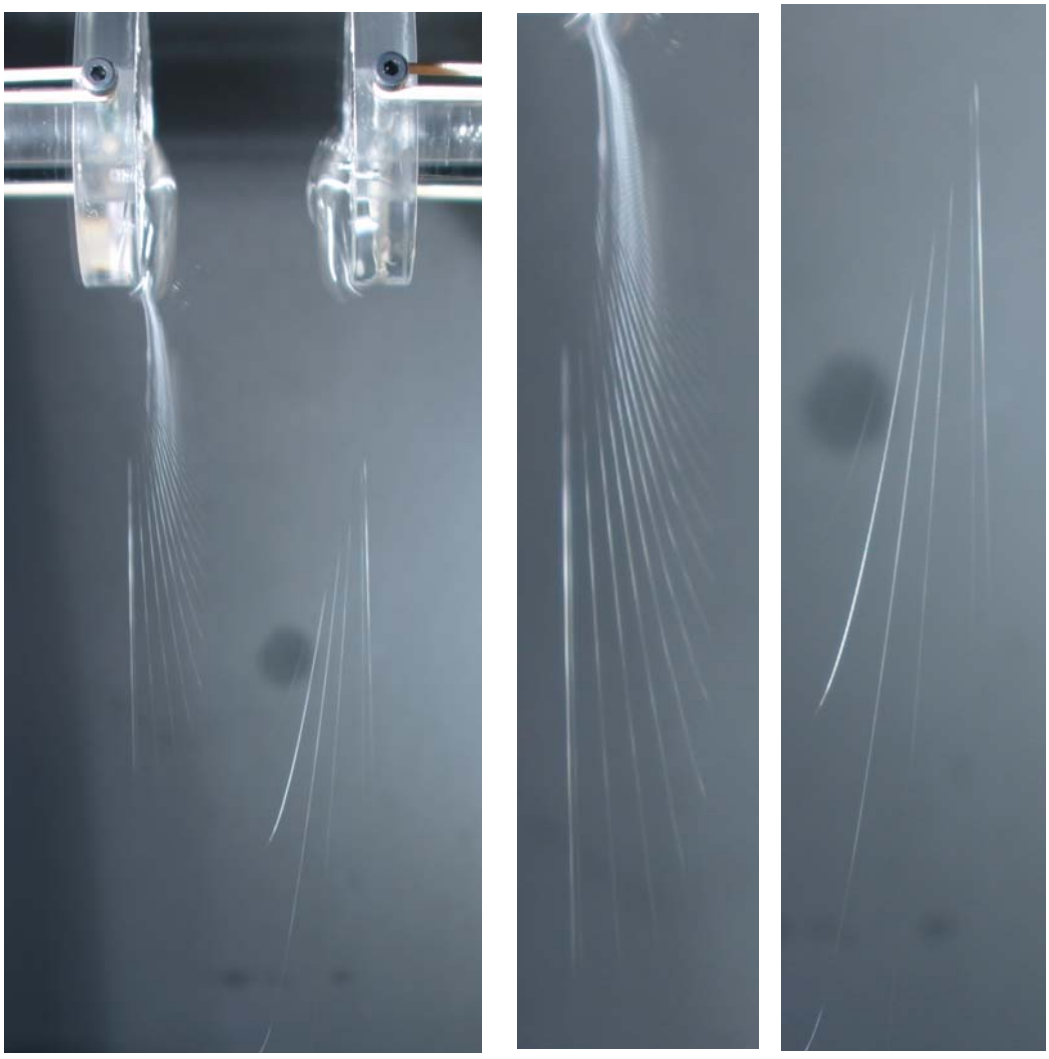

Figure 4.6: Early picture with the strobe to the side. Parts of the filament do not reflect back.

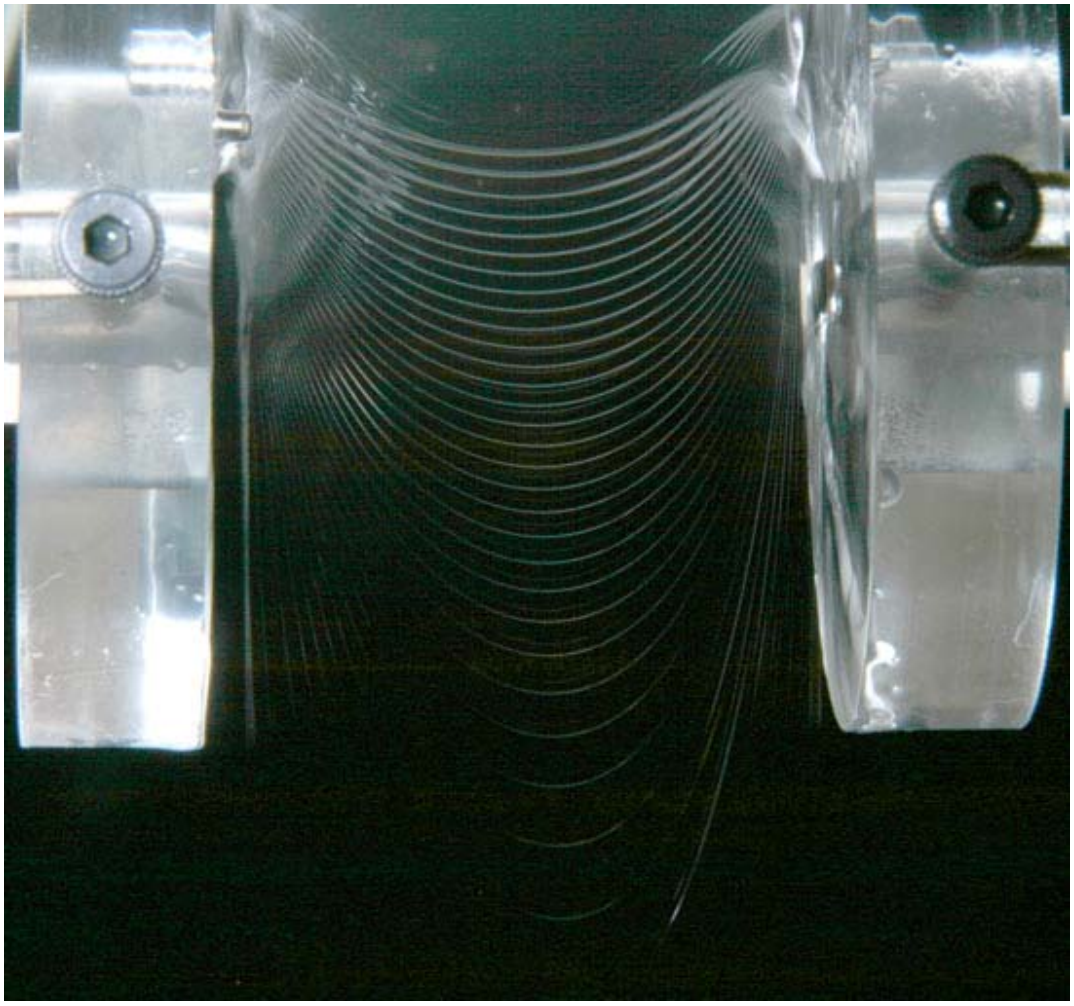

Figure 4.7: Early strobe picture with the strobe close to the oil. The sides lose brightness as the oil moves down but the full filament is clearly visible early on.

To further increase the contrast and make the oil more visible, different backgrounds were tested. Ideally, a material that would reflect as little light as possible was needed. The black construction paper background that was used for months reflected too much light when the strobe was up close, where it illuminated the oil the best. Also, Dr. D. Tanenbaum had introduced me to a very handy program called *Graph Click*, which is capable of finding curves in a picture or graph by detecting changes in color or brightness and returning points all along the curve. This program was capable of saving hours of time spent manually entering points as long as the pictures were clear and had a uniform background. The construction paper did not meet these criteria. I decided to try using polarizer film in front of a white background. That way, with a crossed polarizer

lens on the camera, most of the light reflected off the film could be filtered out. This works very well; most of the unwanted light disappears and the background becomes uniform (Fig 4.8).

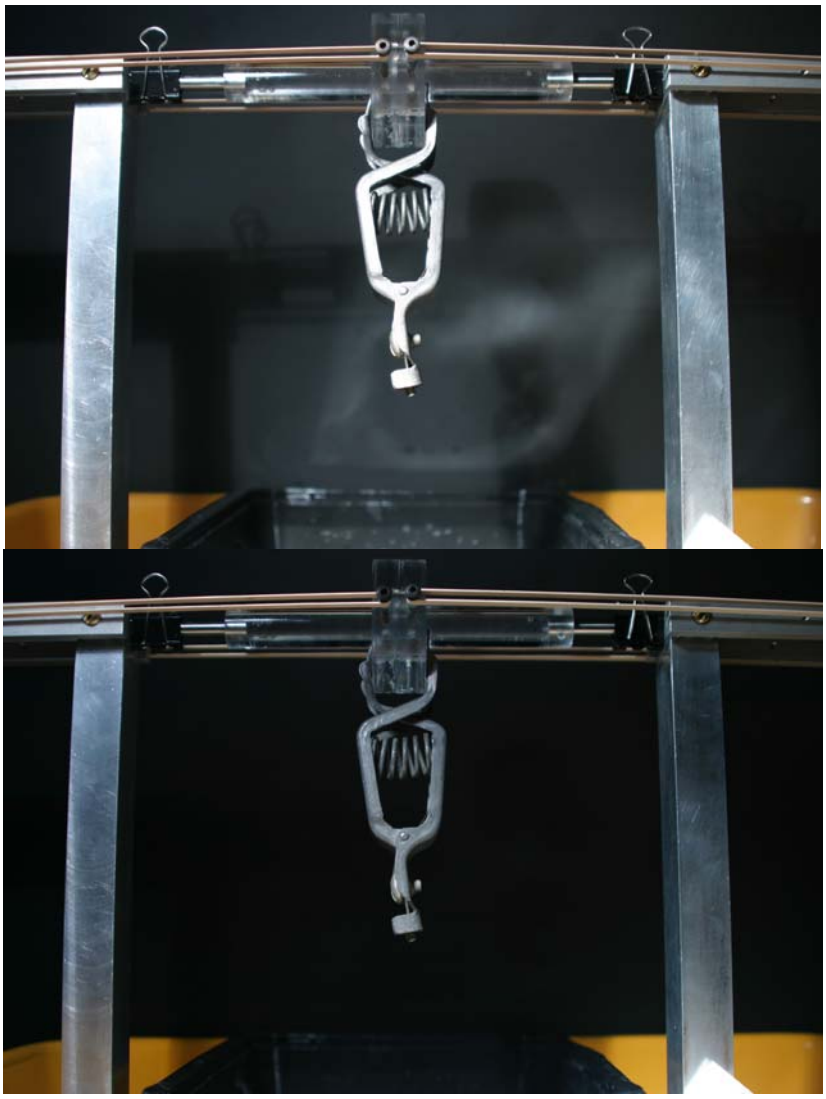

Figure 4.8: Background shot with (bottom) and without (top) cross polarization.

Dr. Tanenbaum also suggested dyeing the oil to see if it helps. Fortunately Dr. Neil Ribe (IGPP, Université Paris VI) had some leftover dye available from his work with silicone oil, which he graciously sent us. The dye comes in the form of powder which dissolves in silicone oil. It gives a red tint to the oil, which made me curious to see if only a white background or a color filter would help. I experimented with both to no

success; the oil appears the best with the polarized background and without a color filter, but the dye does improve the picture (Fig 4.9).

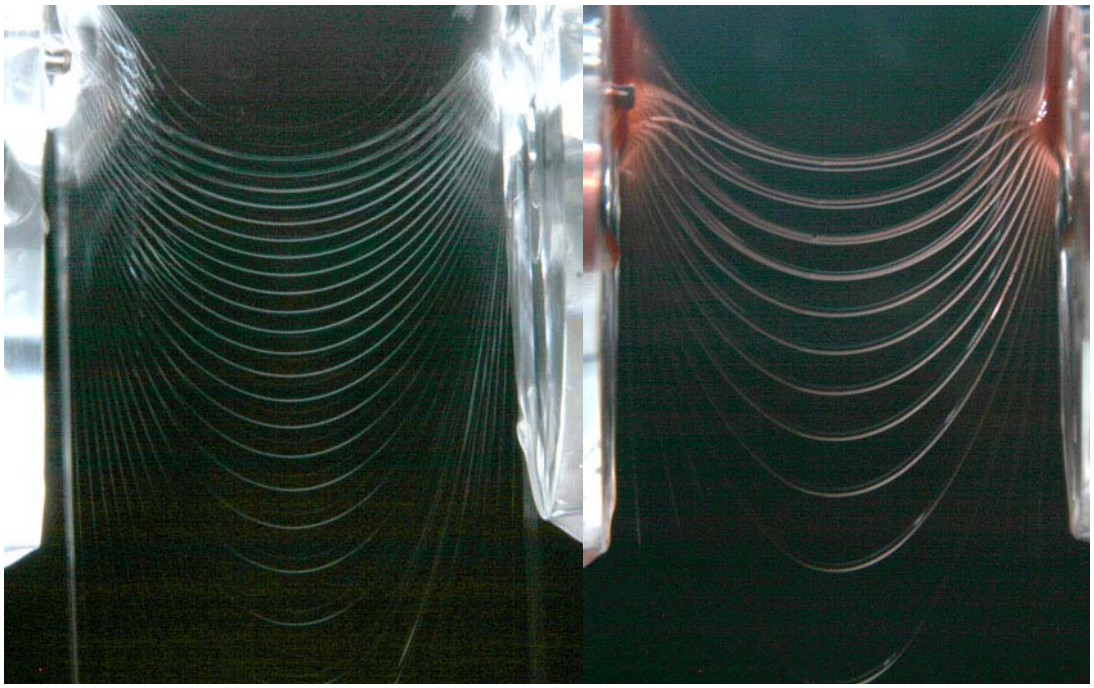

Figure 4.9: Similar runs with and without the dye. Much more detail is visible with the dye.

While testing all these different techniques, I performed numerous runs repeatedly. Filling up the tubes for each run unnecessarily took a lot of time. Instead, I dabbed a little bit of oil on the face of one of the tubes where they normally met and pressed them together. When I released the tubes, they would pull apart, forming a filament between them. This allowed me to perform many runs in a short amount of time. It produced nicely shaped filaments and depending on the amount of oil I applied and the tension in the rubber bands, I could get the filament to evolve any way I liked. This was significantly easier and more efficient so I never went back to the previous method of filling the tubes. The only problem with this is that it is hard to describe how to do it properly because it involves mostly eyeballing the amount of oil used. However, I became good at it and it quickly produces the wanted results, so I ended up using it for my data runs.

4.4 Current Data Taking Process:

Having found the best method to capture the evolution of the filament with the equipment I had available, I was ready to take data. The *Canon EOS 10D* digital camera with a *Canon EF 28-200mm* zoom lens was placed at the minimum focusing distance (~18 inches) away from the plane of the oil, directly in front of where it would fall. The lens was zoomed in all the way so that the region of interest would cover as much of the picture as possible, yielding the highest resolution in that area. The lens was auto focused to the plane of the oil and then set to manual focus so that it would not change when the picture was actually taken. A 8 ½ x 13 inch polarizer film made by *Edmund Industrial Optics* was positioned in the background and the *Hoya PL-CIR* polarizer lens on the camera was aligned so that no light passed through from the background. The strobe, a *Strobotac Stroboslave 1534A*, was placed as close as possible to the area of interest and connected to an *Elenco GF-8036 Function Generator*, which controlled the frequency of the strobe. The function generator was also connected to a *Tektronix CDC250 Universal Counter*, which measured the period of the strobe with an uncertainty of 100 μs.

Figure 4.10: The setup after all the equipment is in place (high resolution on CD).

The period of the strobe was set to be slow enough that the filament would not overlap with itself in the picture but fast enough so that we could capture it as many times as possible. We used periods of 500ms to 800ms between blinks. The camera exposure was set to about 10 seconds for falling filaments and about 30 seconds for breaking filaments so that as much of the evolution as possible was captured. If the filament had fallen outside the field of view of the camera or had broken before the exposure time was up, the strobe was turned off so that no unnecessary light was captured. The aperture was set to around *f*/9.8, which was found to be a good balance for neither overexposing nor underexposing the image. In order to be able to scale the filament, the tubes were always in the field of view of the camera. Precise measurements of the tubes were made with a caliper on both the vertical and horizontal scales that were accurate to .1 *mm*. This allows us to set up a coordinate system in meaningful units when we extract data from the picture.

To take the picture, oil was put on the tubes and the tubes were clamped together. The strobe was set at the proper speed, the camera was focused and adjusted properly, and the lights in the room were turned off. Just as the clamp was released, the camera started taking the picture. After the exposure was done, the lights were turned back on and the process was repeated as many times as was necessary. These raw images were then enhanced in *Adobe Photoshop*, where the levels were adjusted to increase the contrast as much as possible (Fig 4.11 and 4.12). Then the pictures were imported to *Graph Click*, where a scaled Cartesian coordinate system was set up and the coordinates of points along the edges of the filaments and at the midpoints of the filaments were extracted (Fig 4.13). These were with respect to an origin placed on what was estimated to be the axis of symmetry of the filament.

For the falling filament we analyzed, the strobe was running at a period of 0.699 seconds. Boundary data was taken from 8 of the 16 strands visible in the picture because the lower few were not as bright and getting points was more difficult. Midpoint data was taken from all 16. For the breaking filament, the strobe was running at a period of 0.500 seconds. Boundary data was taken from the first 7 of 21 strands and for the remaining 14, points were taken along the middle of the strand because they had gotten too thin to distinguish the top from the bottom.

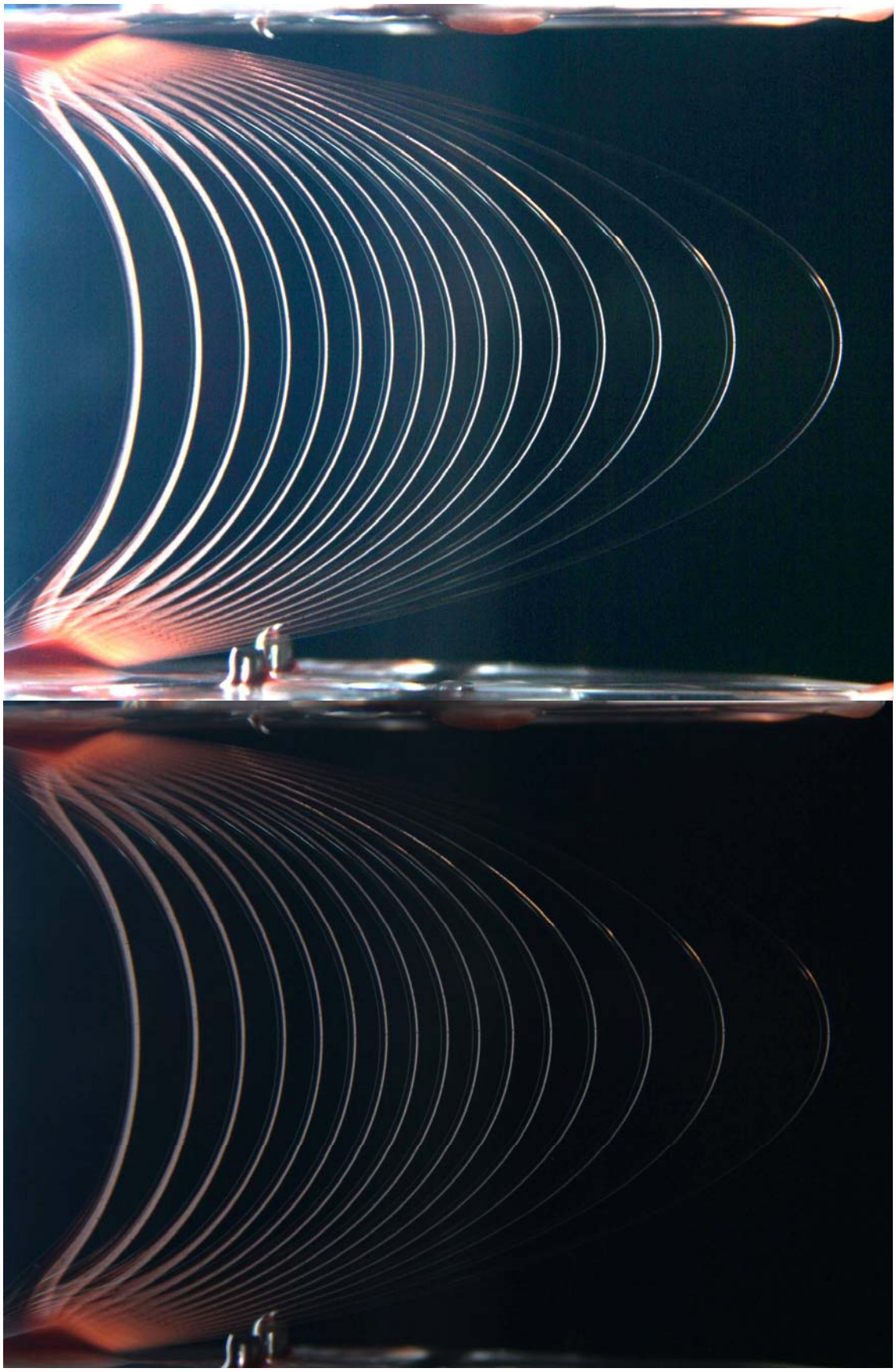

Figure 4.11: A typical falling filament before and after *Photoshop* enhancement. The strobe speed is 0.7 seconds. A high resolution version of the enhanced picture is available on the CD.

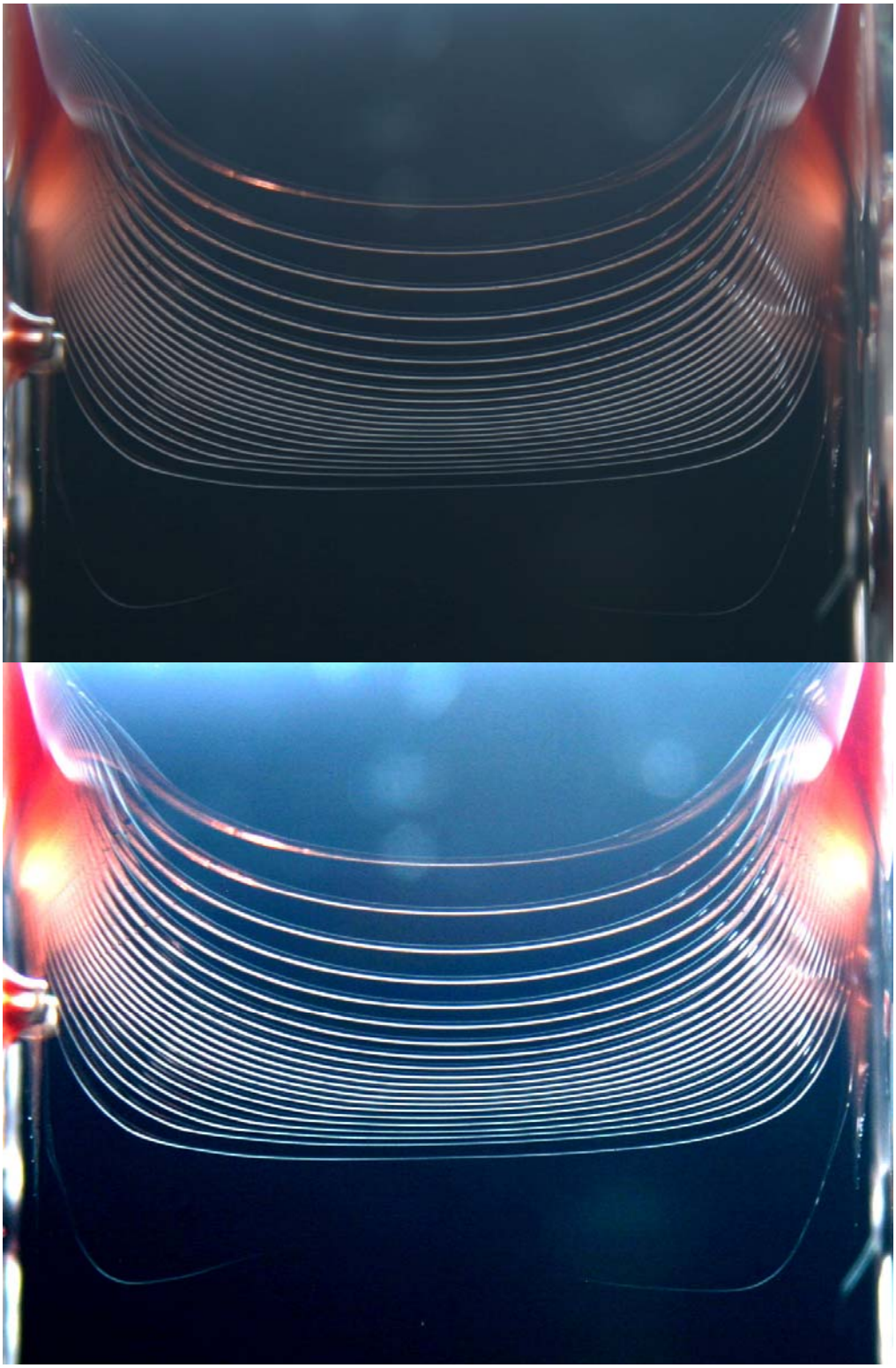

Figure 4.12: A typical breaking filament before and after *Photoshop* enhancement. The strobe speed is 0.5 seconds. A high resolution image of the enhanced picture is available on the CD.

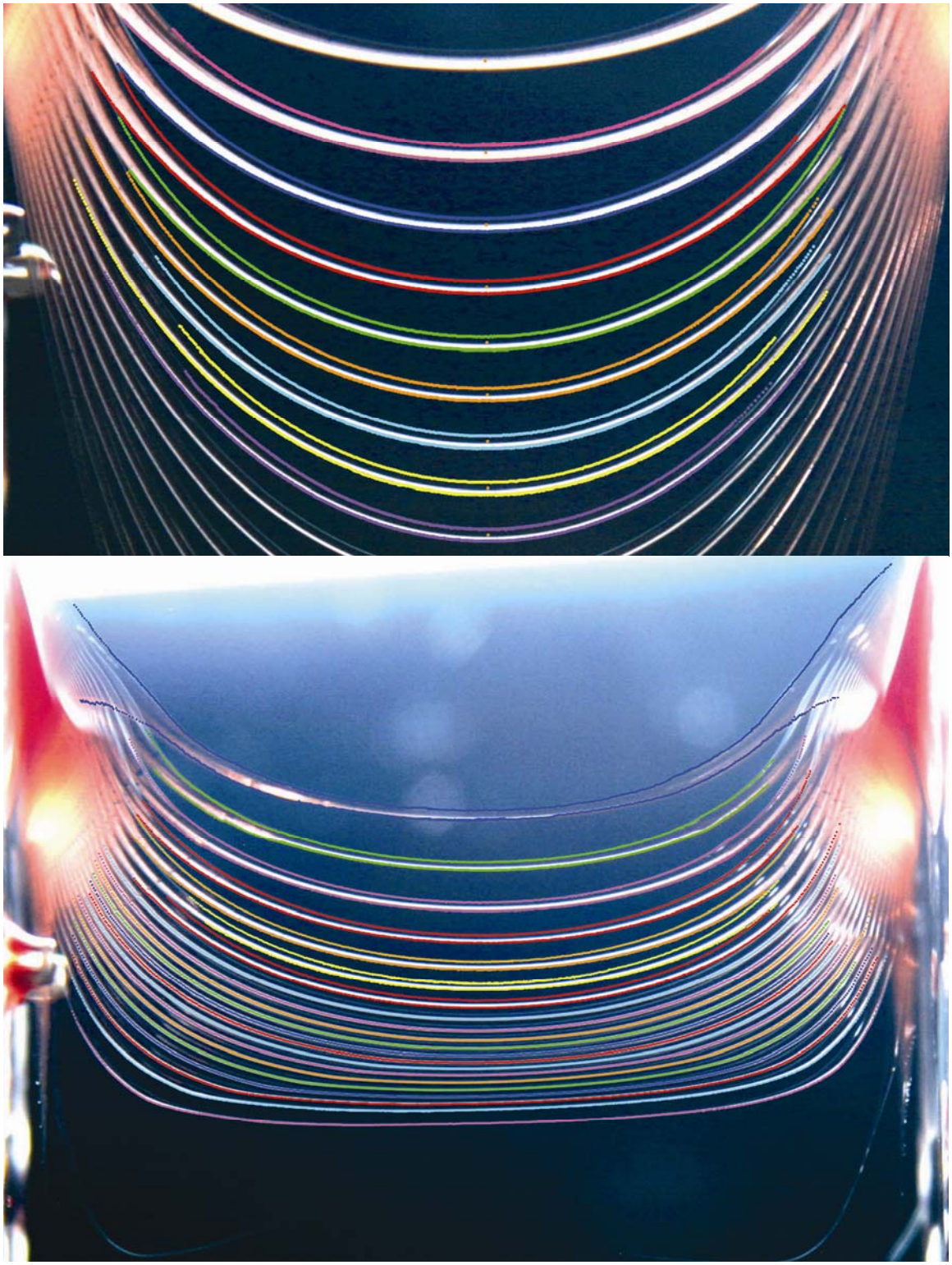

Figure 4.13: A falling and breaking filament with the edge points extracted from *Graph Click* superimposed on the images. High resolution images are available on the CD.

Upon closer inspection of the falling image, there are points visible in the filament, which seem to evolve along with the fluid (Fig 4.14). Several of these points are visible along the filament at random positions. At first we thought these might be bubbles, but we ruled out that possibility because that would guarantee a Rayleigh-Plateau instability and would lead to thinning at those points, which we do not observe. Another possibility is that these points are flakes of dye that have not dissolved. Since the oil is saturated with the dye and there are flakes of dye clearly visible in the oil before it is applied, this seems like a reasonable conclusion.

Although we stumbled on these points by accident, they have proven useful in our analysis of the system. Since they move with the fluid, they follow a path equivalent to a small volume of fluid around that point. They allow us to see how an infinitesimal amount of fluid evolves. Furthermore, since there is no fluid flowing past these points, the volume of fluid between any two of these points must be conserved. This provides a means of testing the functions we calculate for the boundaries. The coordinates of a few sets of these points were extracted in *Graph Click* to serve as endpoints for calculating the volume of fluid between them (Fig 4.15).

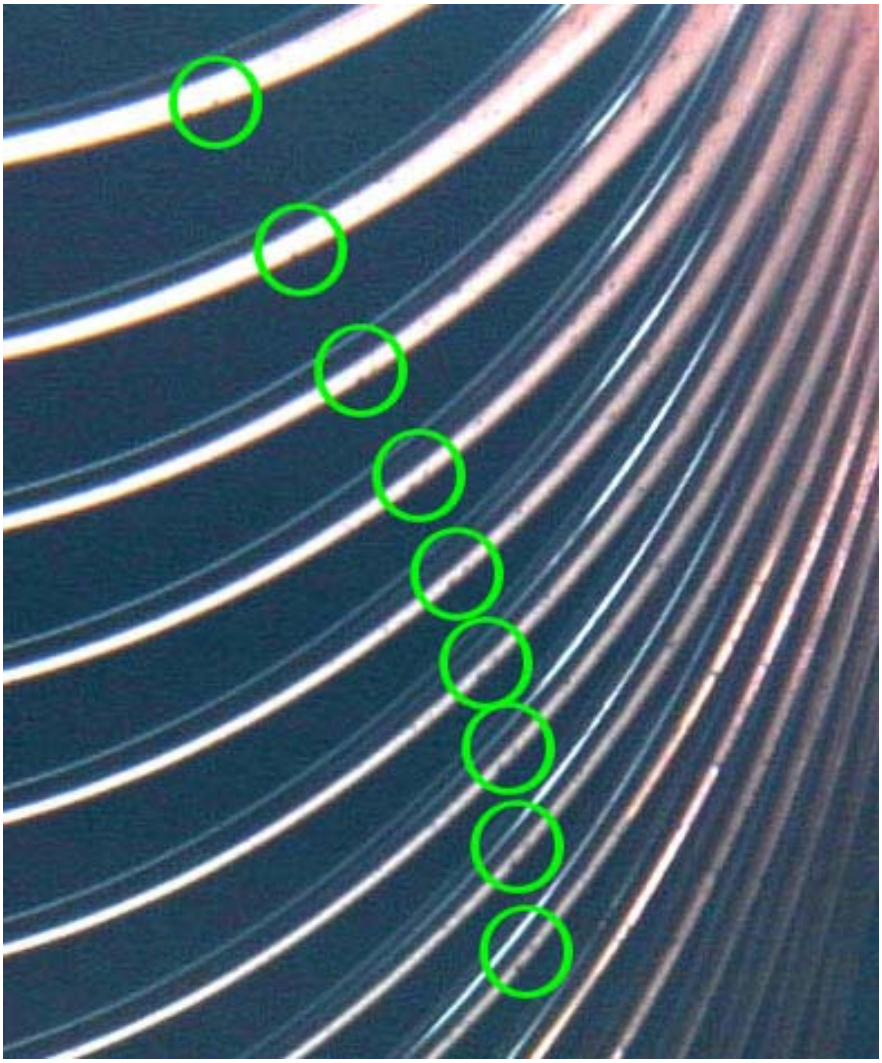

Figure 4.14: Flakes of undissolved dye appearing in the picture.

Figure 4.15: The picture with the position of the dye flakes and midpoints superimposed on it.

5. Comparison with Theory:

5.1 Fitting Functions to the Data:

Since the filament is symmetric, we would like to find an even function that fits our data so that the equations are easier to work with. However, the x coordinates of the raw data from *Graph Click* are with respect to an origin that was only estimated to be on the axis of symmetry, so we needed to find an adjustment for the x coordinate to make the function even. After exporting the coordinates of the edge points to *Microsoft Excel*, I ran a preliminary fourth order polynomial regression on each data set. The fits were good ($R^2 \approx .9998$) and got better for the later strands. This gave me a function of the form

$$y(x') = a' + b'x' + c'x'^2 + d'x'^3 + e'x'^4, \qquad 5.1$$

where *x'* is the horizontal coordinate of the raw data. We find the proper x translation, *k*, by setting the derivative of this function equal to zero and using Newton's method to solve for *k*. Then *x*, the horizontal coordinate for which *y*(*x*) is symmetric, is $x = x' - k$. In terms of the same coefficients *a, b, c, d,* and *e, y(x)* becomes,

$$y(x) = a + bx + cx^2 + dx^3 + ex^4, \qquad 5.2$$

where

$$a = a' + b'k + c'k^2 + d'k^3 + e'k^4, \qquad 5.3a$$
$$b = b' + 2c'k + 3d'k^2 + 4e'k^3, \qquad 5.3b$$
$$c = c' + 3d'k + 6e'k^2, \qquad 5.3c$$
$$d = d' + 4e'k, \qquad 5.3d$$
$$e = e', \qquad 5.3e$$

which gives us our symmetric function.

If our assumption that the filament is symmetric is correct, the coefficients of the odd powers of *x*, *b* and *d*, should be zero. For the 8 strands analyzed, *b* became zero as expected but *d* did not. It did become small, however, and comparing the product dx^3 to the other terms in equation 5.2, it is a couple orders of magnitude smaller. So, while the odd terms did become small, they did not vanish, meaning that there are slight asymmetries in the filament we are analyzing. Graph 5.1 shows the raw data points and the adjusted and unadjusted regressions for the top and bottom of the first strand and Graph 5.2 shows the adjusted form of all the strands.

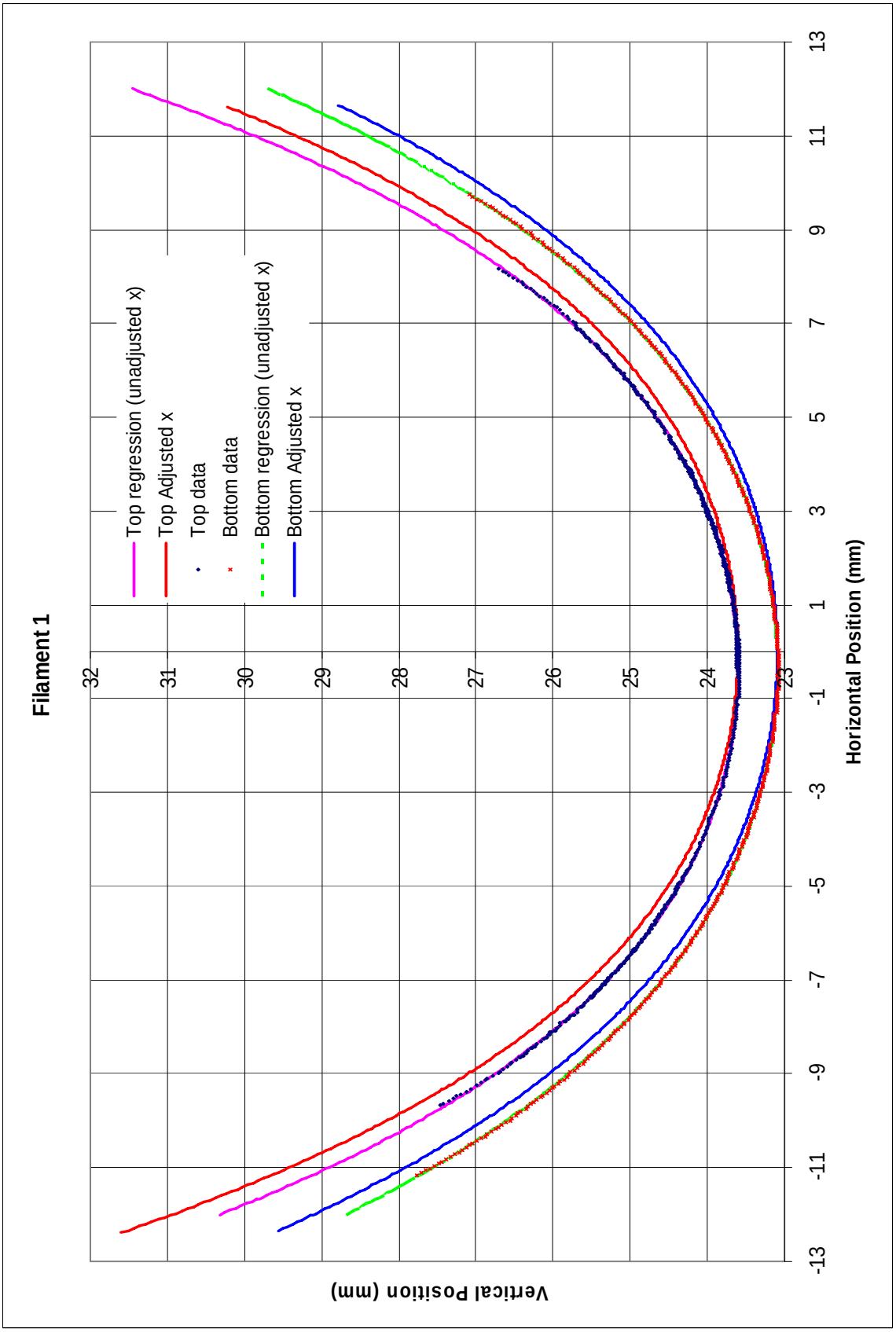

Graph 5.1: Fitting the data and adjusting to make a symmetric function.

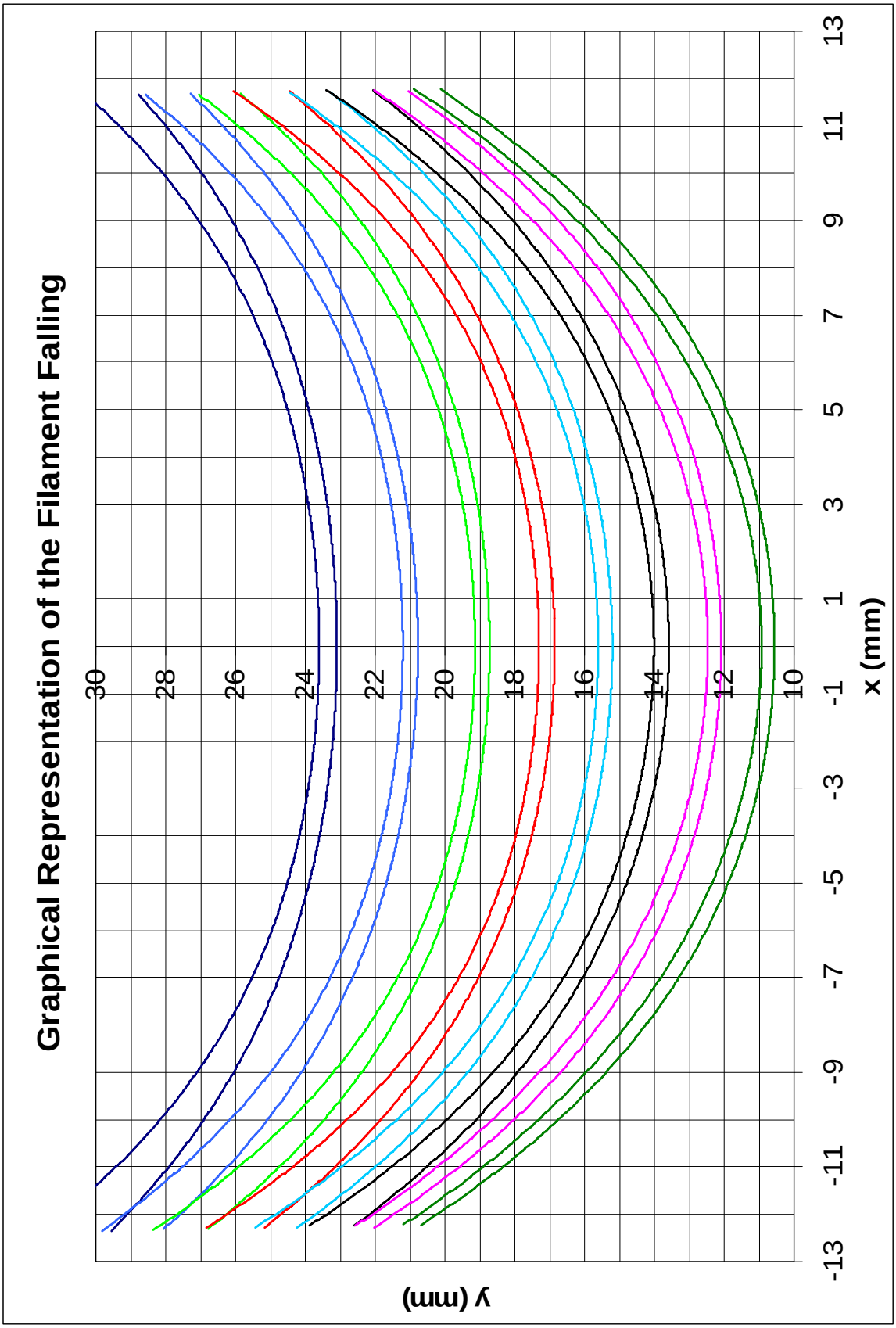

Graph 5.2: A digitized version of the falling filament

Finding a function that fits the endpoint, or dye flake, data was more complicated because the functions were very steep and sometimes curved back on themselves. Instead of running a regression to find *y* as a function of *x*, we were forced to swap the axes and solve for *x* as a function of *y*. Again we used a fourth order polynomial fit which worked very well for all the data sets ($R^2 \approx .9999$). We chose an endpoint function on the left side and one on the right side and found the intersection of these with the boundary functions of each strand using a multidimensional form of Newton's method.

5.2 Conservation of Volume:

If our assumption that there can be no flow in the vein because of its high viscosity and small diameter is correct, then the volume of oil between the two endpoints must remain constant as the filament stretches. To test this, we chose strand 3 and strand 6 to compare. The volume, *V,* is given by

$$V = \frac{\pi}{4}\int_{s1}^{s2} d^2(s)ds = \frac{\pi}{4}\int_{x1}^{x2} d^2(x)\sqrt{1+(\frac{dy}{dx})^2}\,dx, \qquad 5.4$$

where *s* is the arclength coordinate and *d* is the diameter of the filament. Here, *s* should be measured along the centerline of the strand but we can approximate it by using the function we have along the bottom boundary of the strand because the difference is negligible and the error introduced from this is exceedingly small compared to our error from other sources, which I will go into more detail further in this section.

To estimate *V*, we need an idea of how *d* varies over *x*. We measured the diameter of the filament at the endpoints, at *x = 0*, and at halfway between them along *s* by measuring as close as possible to the perpendicular distance between the top and bottom functions (Graph 5.3). This gives us 5 values of *d* for both strand 3 and 6. Initially we assumed *d* had the form

$$d(x) = A + Bx^C, \qquad 5.5$$

where *A* is the value of the top function minus the bottom function at x = 0 and then solved for *B* and *C*. We did this separately for the right and left side of each strand. This worked very well for strand 3; *C* on the right was very similar to *C* on the left (2.635

compared to 2.633). We could not use the same form for d for strand 6 however, because we found that d decreased first by a small amount before increasing (Graph 5.4). This is possibly the early stages of the thinning in the region predicted by Mahadevan. Since variations in the diameter are exceedingly small relative to our measurement accuracy, this could also be an indication of extended constant diameter in the lower region of the strand. Accordingly, we averaged the middle 3 points and assumed d to be constant until the midpoint and then assumed it grew linearly until the endpoint. So for strand 3 we approximated d as having the form of equation 5.5 and for strand 6 as being piecewise, constant at first and then linear.

Having a value for every term in equation 5.4, we approximate V using Simpson's rule. Using a step size of .01 for x and integrating the raw data to the endpoints, the volume comes out to 3.1 mm^3 for strand 3 and 3.7 mm^3 for strand 6.

To estimate the error in V, we moved the endpoints a small but noticeable amount to see how it would affect V. It did not change the value of V significantly. We would have to integrate over about an extra 1.5 mm to make up that much volume, so the bulk of the error was not coming from the location of the endpoints. Looking closely at the data points on the image (Fig 5.1), we notice that the raw data is always one or two pixels inside the filament; it is not exactly on the boundary. For strand 3, the top points are too low and the bottom points are too high by a little over one pixel each. For strand 6, the top points are too low by about one pixel also, but the bottom points are good. Therefore, we are systematically underestimating the volume for both strands, but are underestimating the volume for strand 3 by more. One pixel corresponds with a length of 0.027 mm, compared to our diameter values of around 0.42 mm. For strand 3 this corresponds to underestimating by about 28% and for strand 6 by about 12%. Correcting our volumes by that amount, we get that V is approximately 3.96 mm^3 for strand 3 and 4.14 mm^3 for strand 6. These values are a lot closer than the previous estimate and are within uncertainties of each other.

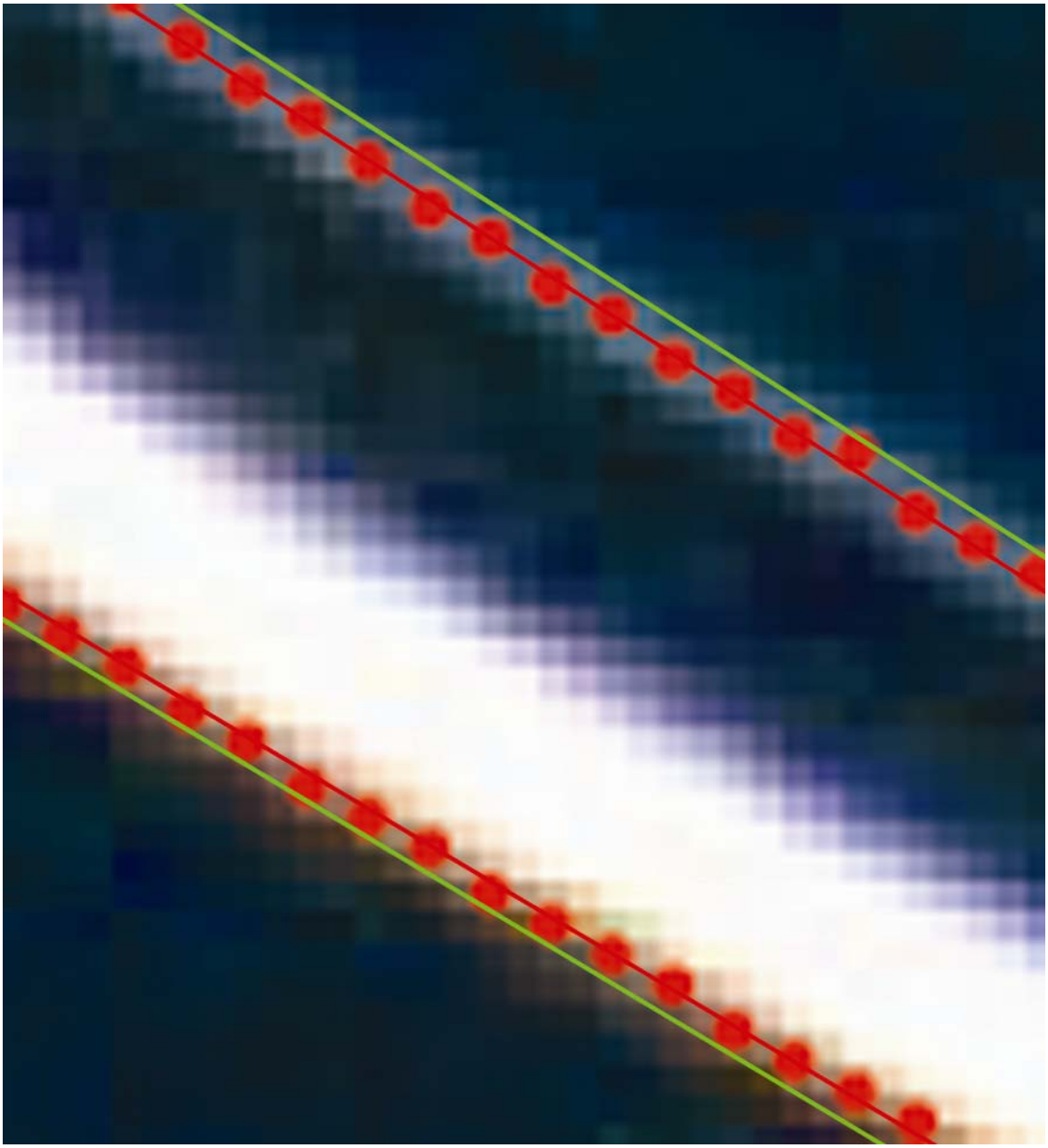

Figure 5.1: An extreme close up of a piece of strand 3. The red points are the raw data points and the green lines are where the red points should be.

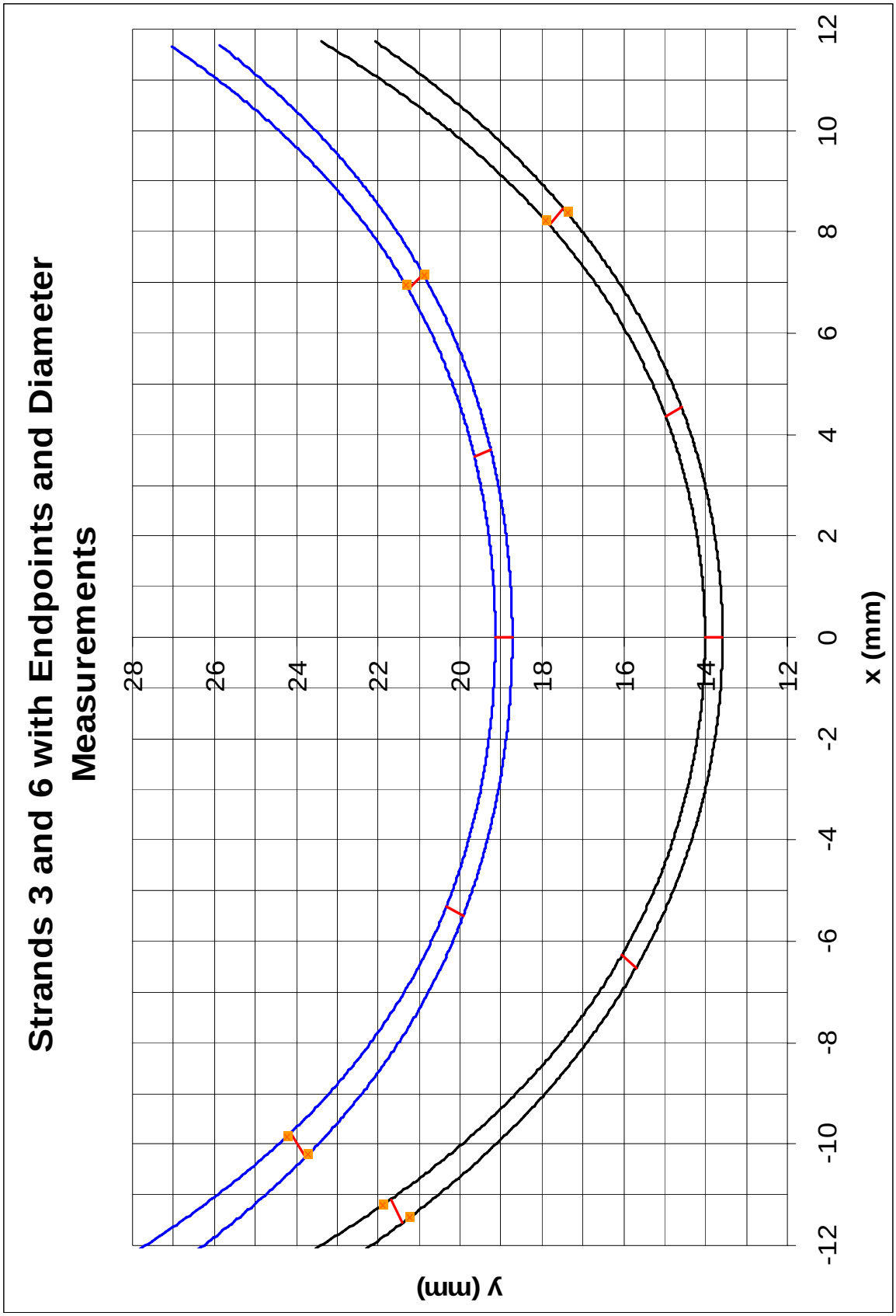

Graph 5.3: Strands 3 and 6 with the diameter measurements and endpoints superimposed.

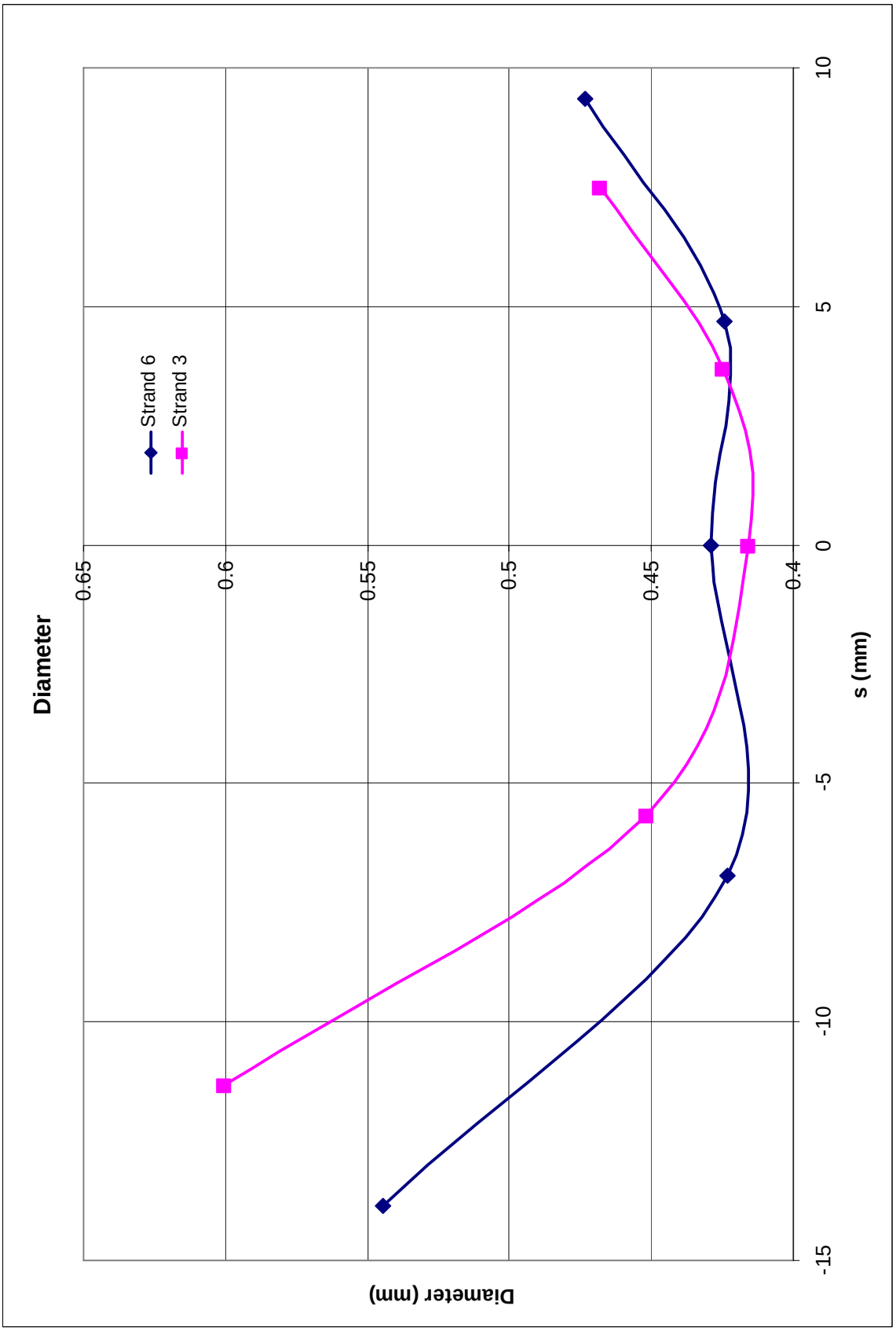

Graph 5.4: The diameter of the filament as a function of the arclength coordinate s.

5.3 Comparison with the Parabolic Approximation:

We are comparing the value of h at time τ as predicted by the parabolic approximation (Graphs 3.2 and 3.3) with what is observed experimentally. Our data points (*y'* and *t'*) are with respect to an initial y_0' and t_0' which are only estimates of the zero points. So, we need a method of solving for $t = t' - t'_0$ and $y = |y' - y'_0|$, where the origin of the unprimed coordinate system corresponds with the initial vertical position and the moment when the oil started falling.

Using our calculation of τ as a function of h, we define a theoretical time $t_{th}(h)$, measured in seconds

$$t_{th}(h) = \frac{\nu}{gL_0}\tau(h)\,. \qquad 5.6$$

We run a regression to find $t_{th}(h)$ as a function of h, where, $h = \frac{y}{L_0}$ is the relative height in units of L_0.

Experimentally we have data from Graph 5.2 at intervals of 0.7 seconds corresponding to a number of successive values of $t' = t + t'_0$. From the same graph, we have corresponding values of $h_{\exp} = \frac{y}{L_0} = \frac{y'_0 - y'}{L_0}$ for each of the successive images with $L_0 = 29\ mm$. From the regression coefficients obtained as in the paragraph immediately above we find $t_{th}(h_{exp})$, and plot t_{th} vs t'.

A graph of t_{th} against t' should be linear, assuming that we have calculated h_{exp}, and therefore $t_{th}(h_{exp})$, using the correct value of y'_0. We have accordingly adjusted y'_0 to the value that makes this graph most nearly linear as illustrated in Graph 5.5 and verified that it yields the best linear fit. Using this value, Graph 5.6 shows the resulting plot of t_{th} vs t' and also provides the intercept correction t'_0. We found our y_0 to be 29.60 mm ±. 0.01mm and our time shift to be .568 s ±. 0.17s.

In order to compare the theoretical timescale with that observed, we would like to compare the value of α obtained experimentally ($\alpha_{\exp}$) with the theoretical $\alpha = \frac{128}{9} \approx 14.22$. The slope of Graph 5.6 is $1/\alpha_{exp}$. This gives us an

experimental α value of 17.81 ±. 0.41 compared with the theoretical value of 14.2. Graphing our data and the theoretical predictions on the same graph with the time axis of the experimental points adjusted by 1/17.81 and the time axis of the theoretical points adjusted by 1/14.2 (Graph 5.7), we see that with this adjustment in the time scale, the experimental data fits very well with the theoretical predictions in this range of values of h. In other words, we are seeing the filament evolve at about 25% slower than predicted.

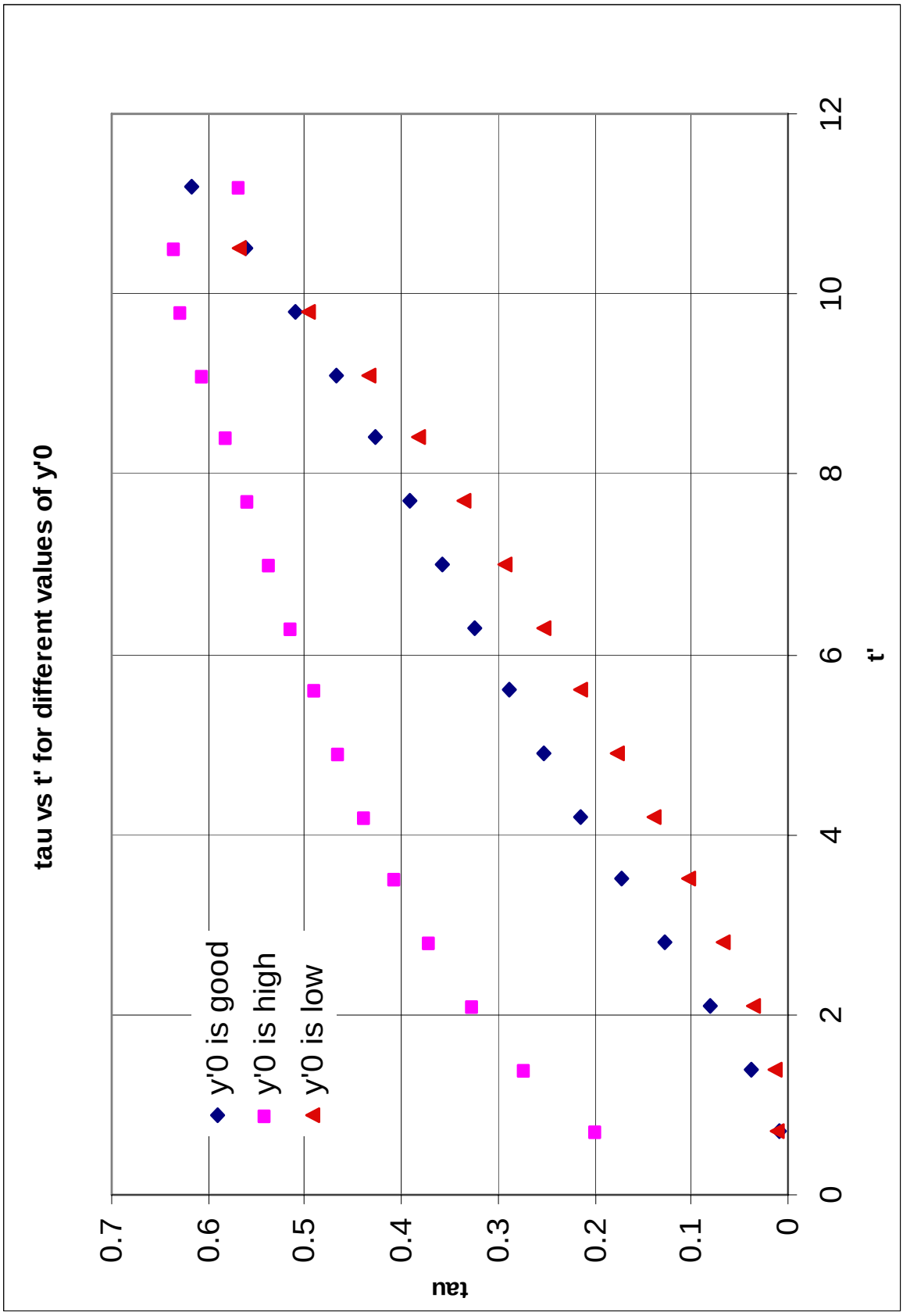

Graph 5.5: Linearizing the graph of tau vs t'

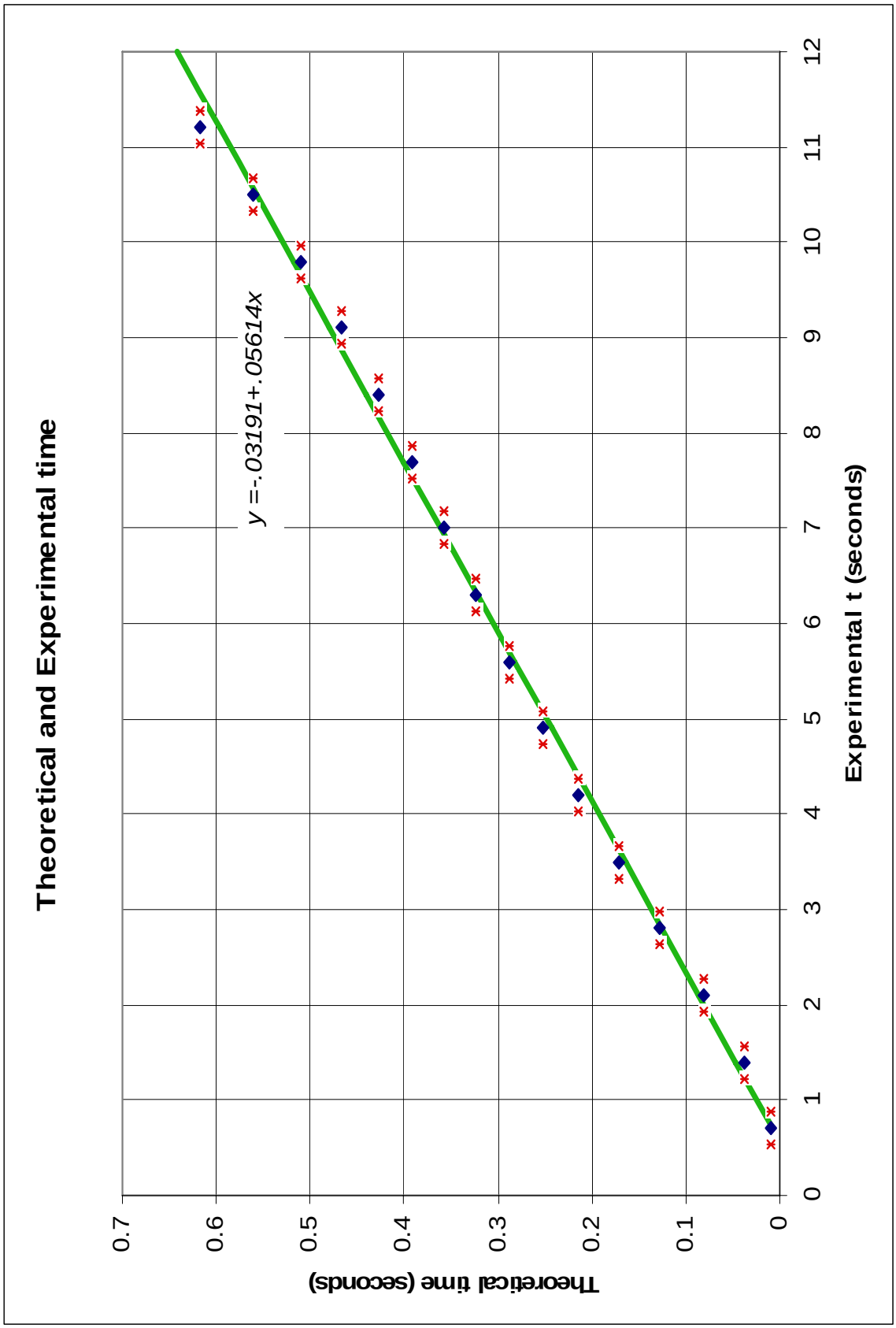

Graph 5.6: Theoretical and experimental time

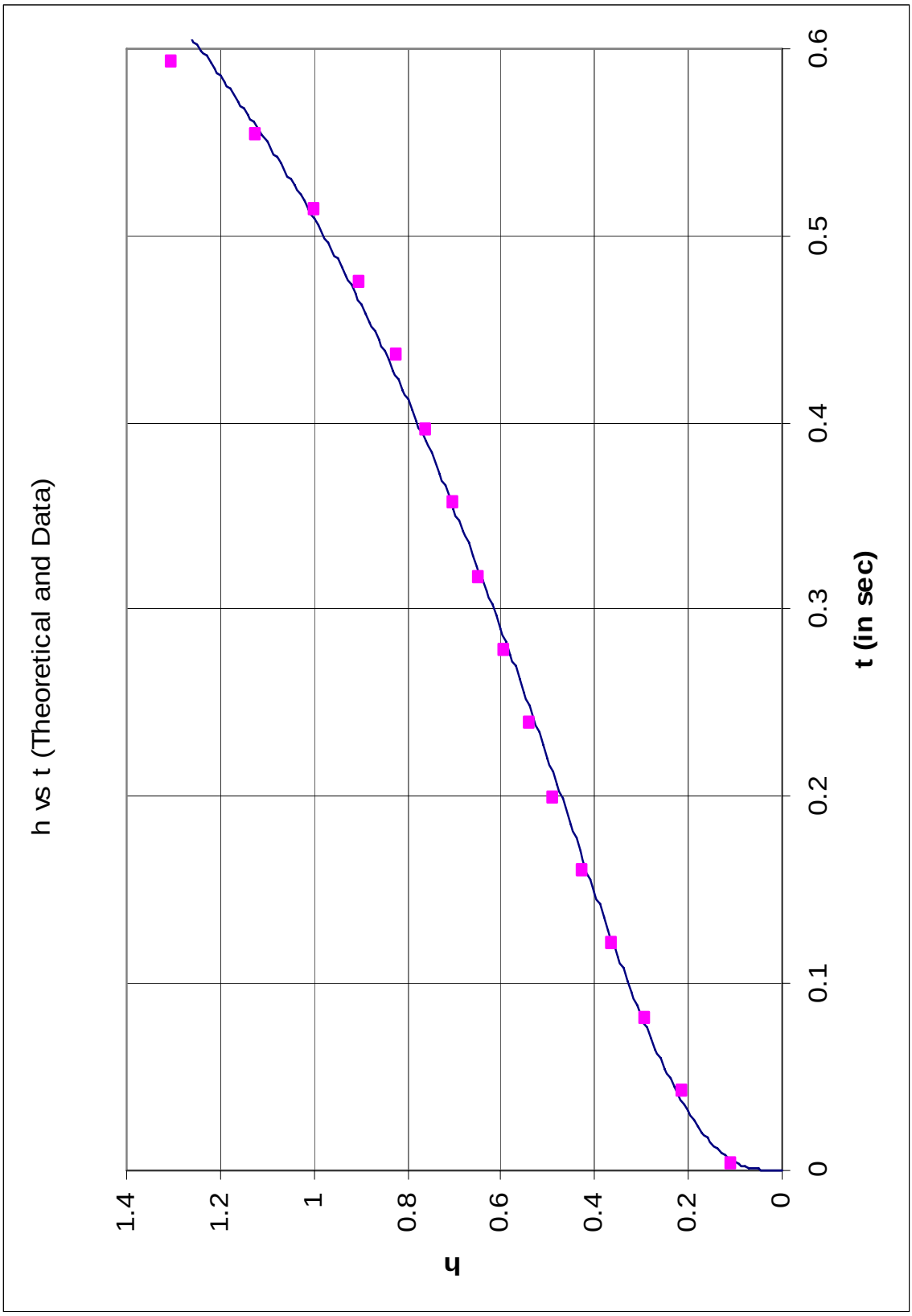

Graph 5.7: Theoretical predictions of the parabolic approximation and our observed values.

6. Conclusions and What is Left for the Future:

We have collected data in the intermediate regime between small deformations and long deformations and have compared it to theory we have developed using a parabolic approximation technique that follows and extends the method Brochard-Wyart and de Gennes have used to approximate the small deformation regime. Collecting more accurate data or data in a different regime will require better equipment and more precise observations.

We have observed three very different behaviors, "falling," "breaking," and "w", of which we only have a qualitative theory for "falling." We cannot enter the "breaking" or "w" regimes using similar methods to those presented here. We have assumed that the filament has a constant radius for most of our analysis, an assumption which we must abandon if we are to make predictions for these more peculiar regimes. It appears evident that these other regimes are governed by the total mass of fluid in the filament. Dr. Neil Ribe has written and sent us Fortran code which factors in changes in radius and may be able to predict these behaviors. As of this moment we have yet to have the opportunity to run it.

As for "falling," the variational techniques used in our analysis seem to predict the behavior fairly well in the region we have observed. However, the filament begins to thin significantly in the region predicted by Teichman and Mahadevan and our assumption that the strand has a uniform thickness breaks down for times just beyond our observations. Our parabolic approximation agrees with the behavior predicted by Brochard-Wyart and de Gennes for short and long deformations but those also do not take into account variations in thickness.

7. Acknowledgements

I would like to thank the faculty and staff of Pomona College, especially Dr. Tanenbaum, Glenn Flohr, and David Haley. Dr. Tanenbaum maintained an interest throughout the year, asking about my progress and making several very helpful suggestions albeit he was busy with his own projects. Glenn spent countless hours crafting every minute part of our apparatus and always had a smile on his face no matter how many times we ask him to change a minor detail. Dave was always around offering his assistance and graciously providing the random equipment as it was needed. None of this would have been possible without these amazing people.

I thank Professor Neil Ribe at the Institut de Physique du Globe for graciously providing us with the dye and computer code modeling the system. The dye has been tremendously useful in collecting our data and has saved me hours of time. I hope to have a chance at running the code soon and seeing the different regimes I have observed experimentally.

I am grateful to Professor Pierre-Gilles de Gennes and Professor Françoise Brochard-Wyart of the Institut Curie in Paris for having taken an interest in my project and developing a more intuitive theory for this interesting system. Our numerous and continuing discussions via Professor Catalin Mitescu have been immensely valuable.

I extend my deepest gratitude to Professor Etienne Guyon of Ecole Supérieure de Physique et Chimie Industrielle and emeritus Director of the Ecole Normale Supérieure (Paris) for making the initial suggestion for this research and for his close and continuing interest and very helpful discussions throughout the length of this project.

I am sincerely indebted to Professor Mitescu who has spent weeks of his time with me in the past summer and year. He has supported me through every step and obstacle of this project, steering me in the right direction and encouraging me to try out my ideas in lab. Because of him, my interest in physics has been renewed. Thank you.

8. Bibliography

[1]Brenner, Michael P., Paruchuri, Srinivas. *Phys Fluids **15:** 113568 (2003)*

[2]Brochard-Wyart, F and P.-G. de Gennes. *Personal Communication*

[3]Chwalek, James M. *et al. Phys Fluids **14:** L37 (2002)*

[4]Ribe, N.M. *Phys. Rev. E **68**: 036305 (2003)*

[5]Ribe, N.M. *Proc R. Soc. London A **460**: 3223 (2003)*

[6]Mahadevan, L., Teichman, J. *J. Fluid Mech. **478**: 71 (2003)*

[7]Maleki, M., Habibi, M., Golestanian, R. *Phys. Rev. Lett. **93:** 214502 (2004)*

[8]Skorobogatly, M., Mahadevan, L. *Europhys. Lett. **52:** 532 (2000)*

[9]Stokes, Y.M., Tuck, E.O., Schwartz, L.W. *Q. Jl Mech. Appl. Math. **53:** 565 (2000)*

9. Appendix

CLEARCO

Product Information

Clearco 100M O- Ring Lubricant

100,000cSt High Viscosity Pure Silicone (CAS#63148-62-9)

4 oz. tube size

Clearco 100M "O" Ring Lubricant is a High Viscosity Polydimethylsilocxane Fluid (CAS# 63148-62-9) that provides Excellent Lubrication in the Assembly of "O" Rings.

This Product is Chemically Inert; it WILL NOT Affect Rubber or EPDM "O" Rings. Clearco "O" Ring Lubricant is Thermally Stable, showing excellent stability when it is exposed to low temperatures for long periods of time.

FEATURES

• **High Viscosity Index Fluid**	• **Chemically Inert**
• **Excellent Lubrication**	• **Excellent Thermal Stability**
• **Non-Flammable**	• **100,000 cSt.. Pure Silicone**

SPECIFICATIONS

Appearance	clear, grease-like paste – odorless & tasteless
Odorless	Yes
Non-Flammable	Yes
Thermally Stable	Yes
Viscosity	100,000cSt.
Availability	12 – 4oz. squeeze tubes per case
Weight	4 lbs. per case
Minimum Order	1 case

O-Ring Compatibility

Aflas (0) Chemraz (4) Kalrez (4) Nitrile, Hydrogenated (4) Polyurethane, Cast (0) Styrene Butadene (4) Buna-N (Nitrile) (4) Epichlorohydrin (4) Fluorosilicone (4) Silicone (2)	Natural Rubber (4) Polyacrylate (4) Polyurethane, millable (4) Teflon, virgin (4) Butyl (4) Ethylene-propylene (4) Hypalon (4) Neoprene (4) Polysuulfide (4) Vamac (4)

(4) Good, both for static and dynamic seals
(3) Fair, usually OK for static seals
(2) Sometimes OK for static seals, not OK for dynamic seals
(1) Poor
(0)No Data

Pricing

1 case (12 tubes)……$8.00 per tube
4 cases (48 tubes)……..$6.00 per tube
12 cases (144 tubes)……..$5.50 per tube
25 cases (300 tubes)……..$4.75 per tube
50 cases (600 tubes)……..$4.25 per tube

1-gallon……$125.00 per gallon
5-gallon container……$110.00 per gallon

FOB Phila, PA USA

For Information & Sample Requests, Contact:

CLEARCO PRODUCTS CO., INC.
3430 G Progress Drive
Bensalem, PA 19020
Tel: 215 639-2640
Fax: 215 639-2919
Email: info@clearcoproducts.com
Web: www.clearcoproducts.com

CLEARCO

Order Toll Free: 800 533-5823

Product Information

Clearco 100,000cSt
High Viscosity Pure Silicone Fluid
(CAS # 63148-62-9)

Clearco 100,000cSt is a High Viscosity Silicone that has a viscosity similar to molasses

Clearco High Viscosity Pure Silicone 100,000cSt Fluid is a 100% Polydimethylsiloxane Silicones (CAS # 63148-62-9) that does not contain additives or solvents. This silicone is **Chemically Inert** to most materials including Rubber, Plastics and Metals. Clearco High Viscosity Silicones are **Thermally Stable**, showing excellent stability when exposed to low and high temperatures for long periods of time. Uses include Damping Fluid –High Temperature Bath Fluid –Hydraulic Fluid – Mold Release Agent - O-Ring Lubricant – General Purpose Lubricant.

FEATURES

• **High Viscosity**	• **Chemically Inert**
• **High Damping Action**	• **Excellent Thermal Stability**
• **Non-Flammable**	• **High Water Repellency**
• **High Resistance to Oxidation**	• **High Compressibility**

SPECIFICATIONS

Chemical Name	Polydimethylsiloxane
INCI Name	Dimethicone
CAS #	63148-62-9
Appearance	Clear, Odorless & Tasteless
Viscosity	100,000cSt
Consistency	Super-thick molasses
Non-Flammable	Yes
Thermally Stable	Yes
Availability	1 – 5 – 55 Gallon Containers
Weight	8 lbs. per gallon
Minimum Order	1 Gallon

Typical Properties

Appearance	Clear
Specific Gravity	0.971
Refractive Index	1.4037
Flash Point (Open Cup) °C (°F)	>326°C (>620°F)
Pour Point °C (°F)	-33°C (-27°F)
Surface Tension @ 25°C	21.5
Operating Temp Range (Open System) °C (°F)	-37°C (-35°F) to 177°C (350°F)
Operating Temp Range (Closed System) °C (°F)	-37°C (-35F) to 232°C (450°F)
Thermal Conductivity (BTU)	0.090
Dielectric Strength (volts/mil)	400

PRICING: 100,000cst

1-gallon container……$125.00 per gallon
5-gallon container……$110.00 per gallon

55-gallon drum……Quote Upon Request

Terms F.O.B. Phila., PA

Also available in 4oz squeeze tubes as 100M O-Ring Lubricant

For More Information or To Request a Sample Contact:

Clearco Products Co., Inc.
3430 G. Progress Drive
Bensalem, PA 19020
Tel: 215 639-2640
Fax: 215 639-2919
Email: info@clearcoproducts.com
Web: www.clearcoproducts.com